Nuclear magnetic resonance measurements of velocity distributions in an ultrasonically vibrated granular bed

PHILOSOPHICAL TRANSACTIONS OF THE ROYAL SOCIETY A MATHEMATICAL, PHYSICAL & ENGINEERING SCIENCES

NMR measurements of velocity distributions in an ultrasonically-vibrated granular bed

Journal:	*Philosophical Transactions A*
Manuscript ID:	RSTA-2013-0185.R1
Article Type:	Research
Date Submitted by the Author:	n/a
Complete List of Authors:	Huntley, Jonathan; Loughborough University, Wolfson School of Mechanical and Manufacturing Engineering Tarvaz, Tahir; Loughborough University, Wolfson School of Mechanical and Manufacturing Engineering Mantle, Mick; University of Cambridge, Chemical Engineering Sederman, Andy; University of Cambridge, Chemical Engineering Gladden, Lynn; University of Cambridge, Chemical Engineering Sheikh, Nadeem; Muhammad Ali Jinnah University, Mechanical Engineering Wildman, Ricky; University of Nottingham, Chemical and Environmental Engineering
Issue Code: Click here to find the code for your issue.:	SHOCK
Subject:	Mechanics < PHYSICS
Keywords:	Granular materials, Rapid granular flow, Vibrated granular bed, Ultrasonic fluidisation, Nuclear magnetic resonance, Magnetic resonance imaging

NMR measurements of velocity distributions in an ultrasonically-vibrated granular bed

J M Huntley[1], T Tarvaz[1], M D Mantle[2], A J Sederman[2], L F Gladden[2], N A Sheikh[3], and R D Wildman[4]

1. Wolfson School of Mechanical and Manufacturing Engineering, Loughborough University, Loughborough LE11 3TU, UK
2. Department of Chemical Engineering, University of Cambridge, Pembroke Street, Cambridge CB2 3RA, UK
3. Muhammad Ali Jinnah University, Department of Mechanical Engineering, Islamabad, Pakistan
4. Department of Chemical and Environmental Engineering, University Park, Nottingham NG7 2RD, UK

Abstract We report the results of nuclear magnetic resonance (NMR) imaging experiments on granular beds of mustard grains fluidised by vertical vibration at ultrasonic frequencies. The variation of both granular temperature and packing fraction with height was measured within the three-dimensional cell for a range of vibration frequencies, amplitudes and numbers of grains. Small increases in vibration frequency were found – contrary to the predictions of classical 'hard-sphere' expressions for the energy flux through a vibrating boundary – to result in dramatic reductions in granular temperature. Numerical simulations of the grain-wall interactions, using experimentally-determined Hertzian contact stiffness coefficients, showed that energy flux drops significantly as the vibration period approaches the grain-wall contact time. The experiments thus demonstrate the need for new models for 'soft-sphere' boundary conditions at ultrasonic frequencies.

Keywords

Granular materials, rapid granular flow, vibrated granular bed, ultrasonic fluidisation, nuclear magnetic resonance, magnetic resonance imaging.

1 Introduction

Rapid flows of granular media occur frequently in nature (for example, avalanches and planetary ring formation) and in technology (for example, the transport of powders in the chemical and pharmaceutical industries). Improved understanding of devastating phenomena such as avalanches, and improved powder-based manufacturing techniques, requires a good understanding of the constitutive behaviour of granular materials in the inertial regime. Some striking similarities with the behaviour of a fluid in thermal equilibrium have been observed, e.g. in its microscopic structure (1), self-diffusion properties (2) and convection behaviour (3), despite the fact that dissipation due to collisions means a source of energy is required to sustain the motion and granular gases are therefore generally far from equilibrium. Theories have been developed relating variables such as packing fraction, granular temperature, shear rate, and heat flux for particular idealized situations such as monodisperse systems as well as some binary systems of hard spherical particles (4, 5).

However, there have been opposing views on the theoretical basis for some even relatively simple phenomena. For example, granular temperature would intuitively be expected to reduce with height above a vibrating base due to the inelastic grain-grain collisions, whereas in practice an upturn in granular temperature near the top of the bed has been observed both experimentally (6-8) and numerically (9-11). One possible explanation (10, 11) arises from the predicted presence of a term in the Fourier heat law related to density gradient, in addition to the usual temperature gradient term (12-15). An alternative explanation for the upturn, however, requires no

such density-gradient term but instead is based on viscous heating associated with compressional pressure waves induced by the moving boundary (16).

Experimental studies on vibrated granular gases have typically used a shaker operating at a few tens of Hz (see, for example, (7, 16)). In the current paper we investigate the effects of increasing the vibration frequency by some two to three orders of magnitude (to a few tens of kHz) through the use of high-power ultrasound technology. NMR measurements are used to probe the time-averaged and through-thickness-averaged distributions of velocity and packing fraction within the three-dimensional bed.

The motivation for this work is threefold. Firstly, the low frequency base of conventional vibrated granular beds acts not only as a means to fluidize the bed but also as a source of pressure waves which can add complexity to the interpretation of the experiments (16). In the example cited above, it is not clear whether the density-gradient term in the Fourier law or the pressure waves are the main cause of the temperature upturn. In order to avoid this complication one requires a vibration period significantly shorter than the Enskog mean free time between collisions, τ_E. Figure 1 illustrates the point showing that this is indeed the case with ultrasound for typical experimental packing fractions and granular temperatures. As a result one is left with diffusion as the primary heat transfer mechanism and one may therefore expect ultrasound sources to act as a more idealized boundary than low-frequency ones, similar to the thermal boundaries sometimes used in simulations.

Secondly, with ultrasound, overlap may occur between the vibration period and the grain-boundary contact time τ_c as shown in Fig. 1. The latter typically ranges from a few μs to a few tens of μs depending on modulus, impact velocity and radius. The grain-boundary interactions may thus become sensitive to the constitutive and geometrical properties of the grains.

Finally, there are now several industrial applications of ultrasonically fluidised granular beds. In the pharmaceutical industry, inhalers have been developed in which ultrasound is used to fluidise a solid bed of dry powder (17). In the case of shot peening, a process that introduces compressive residual stresses into metallic surfaces by repeated impacts with round particles, the particle motion can be sustained by impact with a second surface that is vibrating at frequencies of tens of kHz (18). Improved knowledge of grain-boundary interactions at ultrasound frequencies therefore has the potential to optimise the performance of such processes.

The outline of the paper is as follows. The experimental set up, validation of the cell behaviour and mechanical compression tests to characterize the elastic properties of the grains are introduced in Section 2. Section 3 describes the results of the NMR experiments in which the main cell parameters (number of grains, base velocity and base frequency) are varied systematically. In Section 4, the results of numerical simulations to estimate the effective coefficient of restitution between a grain and vibrating base are presented as part of a wider discussion on the frequency dependence of the results from Section 4, before some concluding remarks in Section 5.

2 Experimental

2.1 Granular material

Most NMR experiments on granular materials use naturally occurring grains such as poppy or mustard seeds because the water or oil within them produce a strong NMR signal (16, 19). For the present work, black mustard seeds were used on account of the relatively large diameter and narrow size range (diameter = 2.30 ± 0.20 mm). The mean grain mass, m, was 6.47 mg. Although not required elsewhere in the paper, the grain-boundary coefficients of restitution were measured using high speed photography as follows: mustard - PEEK 0.71 ± 0.03 mustard - PMMA 0.74 ± 0.02.

The values quoted represent the mean, and standard deviation in the mean, resulting from 10 impacts each.

2.2 Ultrasound source

The ultrasonic vibration source was designed in-house, based on well-established high-power ultrasonic engineering principles (20) and customised to the dimensions of the NMR spectrometer. Figure 2 shows a cross-section through the source. Two back-to-back lead zirconate titanate crystal rings (PZT 806, 54 mm diameter and with a 20 mm diameter central hole, manufactured by Morgan Electro Ceramics, UK), driven by a high voltage sinusoidal waveform, provide the acoustic energy. A steel backplate and aluminium cylinder above, each one quarter of a wave long at the designed resonant frequency of 20 kHz, provide a composite structure with the maximum displacement being produced at the top of the Al plate. An exponentially-tapered half-wavelength aluminium sonotrode then amplifies the motion further due to the reduction in cross-sectional area with height.

In order to transmit the ultrasonic energy from the end of the sonotrode into the measurement volume of the NMR spectrometer, it is necessary to use a waveguide. A set of 18-mm diameter cylindrical rods, manufactured from the polymer polyether ether ketone (PEEK) and joined by stainless steel studding, was used for this purpose. PEEK was chosen over metals such as aluminium to avoid distortions in the NMR signal, which can occur when conductors are near the measurement volume due to eddy-currents induced by the strong time-varying magnetic field gradients. Aluminium waveguides were also found to dissipate a significant fraction of the ultrasonic power when placed in the spectrometer, which is likely to be due to eddy currents induced in the aluminium rod by the travelling ultrasonic waves and the strong static magnetic field. The length of each section of the waveguide was made of an integral multiple of half the wavelength, giving a total waveguide length of 520 mm. The end of the last waveguide, with which the grains made contact, was

machined to a final diameter of 14 mm. The grains were contained within an open-ended cylindrical tube of internal diameter 14 mm made of PMMA supported on the outside of the waveguide with a rubber 'O' ring.

A laser vibrometer (Polytec OFV512 with OFV3001 controller) was used to monitor the surface velocity of the vibrating base. A peak velocity of 4 m s^{-1} was achievable at the design frequency of 20 kHz, although lower values than this were used in the experiments. Measurements were made every mm across the diameter of the cell base to test for uniformity of the vibration amplitude: the variation was found to be within the range ±2% for all the frequencies tested.

Figure 4 shows the experimental arrangement, with the ultrasonic source and waveguide positioned within the NMR spectrometer. The vibrometer beam was directed vertically downwards, through the open cell top, and onto the vibrating cell base by a mirror to allow in situ monitoring of the vibration amplitude.

2.3 Grain-boundary force-deflection curves

The simulations of the grain-base interactions described in Section 4 require an appropriate force-deflection model. The quasi-static mechanical response to diametral compression loading of a set of twelve grains was therefore measured using an Instron testing machine with 50 N load cell. Flat anvils were machined from PEEK to mimic the grain-base contact interactions during the ultrasonic fluidisation experiments.

Figure 3(a) shows a typical force-deflection curve for one of the tested grains. The response is approximately linear, up to a force of around 16 N at which point a sudden load drop indicates that grain fracture has occurred. At lower loads, however, the response is non-linear. Figure 3(b) shows the force (P) versus deflection (δ_z) curves over the range 0 to 0.1 N, together with the best-fit theoretical curve for a Hertzian contact,

$$P = K\delta_z^{3/2}, \tag{1}$$

for three of the grains (the first, 6th and 12th in order of increasing stiffness, K). Over this force range the average best-fit K value over the 12 grains was 1.47×10^7 N m$^{-3/2}$ with a standard deviation of 4.61×10^6 N m$^{-3/2}$. The δ_z values for the horizontal axis of Fig. 3(b) were calculated as one half of the crosshead displacement (to take account of the two contacts in a diametral compression test, as opposed to a single contact for the Hertzian theory) and a shift of the local origin to align it with the onset of loading.

In order to decide which force-deflection law is appropriate to the ultrasonically-fluidised granular medium, i.e. the high-load approximately-linear response of Fig. 3(a), or the low-load Hertzian response of Fig. 3(b), one needs to estimate the maximum contact force during a typical impact. Assuming that Hertzian impact theory is applicable (21), the maximum contact force P_m during an elastic impact for a grain with mass m and incoming velocity V_z is

$$P_m = K^{2/5}\left(\frac{5mV_z^2}{4}\right)^{3/5}. \qquad (2)$$

Substituting the values $K = 1.47\times10^7$ N m$^{-3/2}$, $m = 6.47$ mg, and a typical impact velocity V_z of 0.2 m s^{-1} results in a P_m value of 0.094 N. The force range shown in Fig. 3(b) is therefore applicable to the current situation, thus justifying the use of Eqn. 2 above and the subsequent analysis in Section 4.

2.4 NMR acquisition

A novel spin-echo velocity profiling technique was previously developed by the authors and described in Refs (22),(16). This allows velocity distributions within a three-dimensional cell to be measured as a function of both vertical position (z) and phase of a low-frequency vibration. In the current study, the vibration frequency is too high to allow time-resolved measurements of velocity and temperature; the pulse sequence was therefore not triggered in any way.

The pulse sequence used in this study was that previously described in (22). We chose here the vertical velocity component (v_z) since the granular temperature is normally

highest in this direction, although other components could be measured equally easily at the expense of additional acquisition time. The measured signal integrates through the thickness of the cell; in effect we traded spatial resolution in the horizontal directions (x or y) for the z and v_z resolution that are the primary focus of this paper. Previous studies on 2-D and 3-D vertically vibrated beds using high speed photography and PEPT (3, 7) have demonstrated that the main gradients in temperature and packing fraction occur along the z direction, with relatively minor perturbations in the horizontal directions.

All MRI experiments were acquired on a Bruker Biospin DMX 300 spectrometer operating at a ^{1}H frequency of 300.13 MHz. Spatial resolution was achieved using a three-orthogonal axis gradient system capable of producing a maximum gradient strength of 1 T m^{-1}. The field of view in the z-direction was 40.0 mm and the number of data points acquired was 128, thereby giving an axial pixel resolution of δz = 313 μm.

A 25 mm ^{1}H birdcage resonator was used to excite and detect the magnetisation from the mustard seeds and the ^{1}H 90 degree pulse length was 32 μs. The NMR pulse sequence of Mantle et al. (22) has two distinct advantages over a single-spin or stimulated-echo velocity profile sequence (used by, for example Huan et al. (8)): (i) it refocuses magnetisation dephasing due to constant motion in a linear background gradient (23); (ii) the readout, or spatially encoding, gradients are also compensated for velocity artefacts. Ramped gradients were used throughout to minimise extra spin de-phasing from magnetic fields created by eddy currents due to gradient switching. The gradient ramp-up and ramp-down times were 100 μs. The total echo time TE was 2.14 ms. Velocity encoding was achieved by using 64 equal gradient increments from -0.8 T m^{-1} to +0.8 T m^{-1}.

The length of the velocity encoding gradient, δ, was 455 μs. The delay between velocity encoding gradient pulses, Δ, was 1.20 ms. Sixty four scans for each velocity

encoding increment, at a recycle time of 365 ms, were averaged to obtain a sufficient signal-to-noise ratio. Hence the total experimental time for a single vibration frequency was approximately 25 minutes. Following acquisition, the raw data was zero-filled to 256 data points in the velocity encode dimension, and then a 2-dimensional Fourier transform was applied to each set of data to give spatially encoded velocity profiles, denoted here by $S(v_z,z,)$. These parameters enable the determination of velocities within a range –0.875 m s^{-1} to + 0.875 m s^{-1}, with a resolution of 0.007 m s^{-1}.

3 Experimental results

Three groups of experiments were carried out. In the first, the number of grains, N_g, and frequency of the ultrasound, f, were fixed whilst the peak base velocity, V_b, was varied. In the second, N_g was varied whilst the other parameters remained fixed. Finally, in the third group, the ultrasound frequency was varied together with the displacement amplitude so as to maintain a constant peak base velocity. This was possible because although the ultrasound source was designed for a fixed frequency, it was found to have significant resonances at other frequencies.

3.1 Effect of varying the base velocity

Three different base velocities were used: V_b = 0.33, 0.50 and 0.74 m s^{-1}. Figure 5 shows the measured time-averaged raw signal $S(v_z,z)$ for each with N_g = 40 and f = 11.1 kHz. Within each image the central 'blob' is the signal from the mustard grains, and the vertical and horizontal axes represent respectively z (height above the base) and v_z (the vertical velocity component).

A slice through an image at a given height provides a signal proportional to the probability density function (PDF) for v_z at that height. Figure 6 shows three examples of such PDFs from Fig. 5(c) at heights z = 4, 8 and 16 mm. Superimposed on the

experimental PDFs are Maxwellian distributions produced by fitting the curves defined by

$$S_f(v_z, z) = \frac{C_1}{\sqrt{2\pi}\sigma} \exp\left(-\frac{\left(v_z - \langle v_z \rangle\right)^2}{2\sigma^2} \right) + C_2 , \quad (3)$$

to $S(v_z,z)$ on a row by row basis. The parameters C_1 (the peak amplitude), C_2 (the average signal offset due for example to background noise), σ (the peak width) and $\langle v_z \rangle$ (the velocity offset) are in general functions of z. The closest match between the experimental and best-fit curves is at high altitudes; this is to be expected because distortions to the PDF due to interaction with the base have been largely randomized through intergrain collisions. As the altitude is reduced, progressively larger deviations are seen, notably the appearance of a 'shoulder' centred around v_z = +0.4 m s^{-1} in Figure 6(a). Such distortions were also noted in previous low-frequency experiments (16) and were explained as being due to the energetic particles that had just left the base in the $+v_z$ direction.

Profiles of the z-component of the granular temperature, and the packing fraction, may be estimated from the best-fit parameters as

$$T_z(z) = \sigma^2(z) , \quad (4)$$

and

$$\eta(z) = \frac{N_g d^3}{6R^2} \frac{C_1(z)}{\int_0^\infty C_1(z) dz} , \quad (5)$$

respectively, where d is the grain diameter and R the radius of the cell (16). These profiles are shown in Fig. 7 for the three datasets from Fig. 5. The temperature profiles show only a weak dependence on height. There is a hint of an upturn in the two highest velocity profiles at high z, although this is the region where the uncertainty is greatest due to the lower signal levels. The packing fraction profiles are

qualitatively consistent with previous studies (e.g. (6, 7, 16)), with a rapid increase to the maximum density a short distance above the base, and then an approximately exponential decay with z at higher altitudes.

A simple scaling relation to model the change in mean temperature of the bed with V_b and N_g was proposed in the 1990s as follows (7, 24):

$$T \propto \frac{V_b^{\alpha}}{N_g^{\beta}}, \tag{6}$$

where $V_b = A_0\omega$, with A_0 the displacement amplitude of the vibration and $\omega = 2\pi f$ its angular frequency, and α and β are two empirically-determined scaling exponents. Typical α values reported in the literature range from 1.2-1.9 and β values from 0.3 to 0.8 (6).

A density-weighted average temperature was calculated from the temperature and packing fraction profiles and then plotted on logarithmic axes in Fig. 8(a), in non-dimensional form, to allow an estimate of the scaling exponent α to be obtained for the ultrasonically-vibrated bed. Non-dimensional temperature T_z^* is defined as follows:

$$T_z^* = T_z / gd . \tag{7}$$

The best-fit value for α of 0.90 is somewhat lower than previously reported values from the literature at low frequency, however the small number of data points plus the scatter about the best-fit line mean there is significant uncertainty in this parameter.

3.2 Effect of varying the number of grains

Three experiments were carried out with the values N_g = 20, 40 and 60, the other main parameters being held constant (f = 11.1 kHz, and V_b = 0.74 m s^{-1}). Figure 9 shows the resulting signal $S(v_z,z)$ for the three cases. As more grains are added, both the height of the bed and the width of the velocity distribution are reduced. This can be

understood qualitatively as a consequence of the increased number of dissipative grain-grain collisions that occur, on average, between the energy-injecting grain-base collisions. The density-weighted average temperature, calculated as described in the previous section, is plotted in Fig. 8(b) as a function of N_g. The straight line fit corresponds to a scaling exponent $\beta = 1.25$.

3.3 Effect of varying the frequency of the base

The ultrasonic source had a resonance at 20.2 kHz, close to the design frequency of 20 kHz, but also at several additional frequencies including 11.1 and 17.7 kHz. A_0 was varied so as to keep V_b constant at 0.74 m s^{-1} for all three experiments. According to classical energy flux boundary conditions (see for example (25)), the key parameter associated with the motion of the boundary is its root mean square velocity. All three experiments should therefore have resulted in the same level of fluidisation, if such classical formulae are applicable at ultrasonic frequencies.

It is clear from the results, however, presented as $S(v_z,z)$ in Figure 10(a)-(c), that there is a dramatic reduction in the granular temperature of the bed as f is increased from 11.1 kHz to 20.2 kHz. A possible explanation for this phenomenon is that at ultrasonic frequencies the period of vibration $T = 1/f$ may become comparable to the contact time, τ_c, whereas in the derivation of the boundary conditions it is implicitly assumed that τ_c is sufficiently small to be neglected. The overlap between T and typical τ_c values is illustrated in Fig. 1 with the other relevant timescales.

The duration of an elastic collision for a particle with incoming velocity V_z is given by

$$\tau_c = 2.87\left(\frac{m^2}{rE^{*2}|V_z|}\right)^{1/5} \tag{8}$$

where

$$\frac{1}{E^*} = \frac{1-\nu_1^2}{E_1} + \frac{1-\nu_2^2}{E_2}\,. \tag{9}$$

and r is the radius of the grain. Variables E and ν represent Young's modulus and Poisson's ratio, respectively, with subscripts 1 and 2 referring to the grain and the boundary. In order to estimate τ_c for the current situation we therefore require a value for E^*. The results of the experiments in Section 2.3 provide this information because E^* is related to the measured Hertzian stiffness coefficient, K, as follows:(21)

$$K = \frac{4}{3} r^{1/2} E^* . \tag{10}$$

Combining Eqns. (8) and (10) with the value K = 1.47×10^7 N m$^{-3/2}$, and a typical impact velocity V_z of -0.2 m s^{-1} results in a τ_c value of 51 μs. This is indeed comparable to the period of 50-90 μs for the vibration frequency range of 11-20 kHz. For this reason, simulations have been carried out to estimate the frequency dependence of the average increase in speed of a grain due to a grain-boundary impact. The approach used and the results are summarised in the next section.

4 Numerical simulations of grain-boundary interactions

A full analysis of the granular temperature distribution within the bed is beyond the scope of the current paper; we focus instead on estimating the changes in average rebound velocity with frequency for a single impact. Analysis of a particle interacting with a base undergoing 'sawtooth' motion has been carried out by Warr *et al*. for the case of instantaneous collisions (26). The finite-contact-time problem is much more difficult to solve analytically. A model was therefore developed in which the one-dimensional equation of motion for a particle approaching a vibrating base in the vertical direction is solved numerically.

Applying Newton's second law with the Hertzian force-displacement law (Eqn. (1)), and neglecting gravity for the duration of the impact, the position of the centre of mass of the grain, z_c, is given by the 2nd order nonlinear ordinary differential equation:

$$\frac{d^2 z_c}{dt^2} = \frac{K}{m}(z_b - z_c + r)^{3/2} H(z_b - z_c + r) \tag{11}$$

where z_b is the position of the base:

$$z_b = -A_0[\sin(\omega t + \phi) - 1], \tag{12}$$

t is time, ϕ is a phase offset and $H(z)$ is the Heaviside step function ($H(z) = 1$, $z \geq 0$; $H(z) = 0$, $z < 0$). No loss terms are included in Eqn. (11), so that in the absence of vibration ($A_0 \to 0$) the rebound speed equals the speed of approach, i.e. the coefficient of restitution $\varepsilon \to 1$.

Equation (11) can be simplified by the substitution of the variable $z = z_c - r$ as follows:

$$\frac{d^2z}{dt^2} = \frac{K}{m}(z_b - z)^{3/2}H(z_b - z). \tag{13}$$

z can be thought of as the position of a particle of zero radius, which allows the grain and base trajectories to be plotted on the same axes.

Equation (13) may be redefined as two first order ordinary differential equations in the variables $z_1 = z$ and $z_2 = dz/dt$, which can then be solved using standard 4th order Runge-Kutta techniques (27). The initial conditions are $z_1(0) = 0$, $z_2(0) = -V_z$, and a time step of $\tau_c/100$ was used for all the results presented here.

Typical impact trajectories are shown in Figure 11 for three different base frequencies, with an arbitrary phase offset $\phi = 0.1$. Repeated impacts are apparent in the two higher frequency cases before the grain passes back upwards through the position $z = 0$. Integration is terminated at this point, with the value of z_2 here allowing an effective coefficient of restitution to be calculated as

$$\varepsilon_e = -z_2^+(0)/z_2^-(0). \tag{14}$$

Superscripts + and – indicate the sign of z_2, and thus refer to the post- and pre-impact velocities, respectively.

ε_e is an indicator of the energy injected into the bed, with larger values expected to produce a higher level of fluidisation than smaller ones. We use this therefore as a measure of the effectiveness of the vibrating base at different frequencies whilst maintaining a constant peak base velocity $V_b = A_0\omega$.

The phase of the base relative to the time at which the particle passes downwards through $z = 0$ is essentially random because of the very large number of base cycles between successive base-grain impacts. Simulations were therefore done over 16 values of ϕ uniformly distributed over the range 0 to 2π. Figure 12(a) shows the average ε_e from the 16, with error bars indicating the standard deviation, for the case V_b = 0.74 m s^{-1}. Experimentally-determined values of K and m were used throughout.

At low frequencies, ε_e is seen to be independent of frequency, consistent with standard boundary conditions where V_b is the sole dynamic parameter controlling energy flux(25). At very high frequencies, $\varepsilon_e \to 1$, the same value as for a stationary base. The intermediate region, where the vibration period is comparable to the impact duration, is where ε_e is changing most quickly with f. The two relevant frequencies, f = 11.1 and 20.2 kHz, have ε_e values of 3.04 and 1.63, respectively. The approximate halving of rebound velocity (and corresponding reduction in energy input by ~80%) thus provides a plausible explanation for the strong reduction in level of fluidisation between Fig. 10(a) and 10(c).

In order to generalise the results to other granular materials, base velocities and approach velocities, it is convenient to recast Eqns. (12) and (13) in non-dimensional form. Time and frequency are normalised using the contact time, τ_c, so that $t^* = t/\tau_c$ and $f^* = f\tau_c$, where superscript '*' is used to denote a non-dimensional variable. Displacements z and z_b, and amplitude A_0, are normalised using the maximum indentation depth, z_m, which occurs at the maximum contact force P_m during an elastic impact on a stationary base:

$$z_m = \left(\frac{5mV_z^2}{4K}\right)^{2/5}. \qquad (15)$$

In non-dimensional form, Eqns. (13) and (12) then read respectively

$$\frac{d^2z^*}{dt^{*2}} = C(z_b^* - z^*)^{3/2}H(z_b^* - z^*) \tag{16}$$

and

$$z_b^* = -A_0^*[\sin(\omega^* t^* + \phi) - 1], \tag{17}$$

where $\omega^* = 2\pi f^*$, C = 10.84 and

$$A_0^* = V_b^*/\omega^* . \tag{18}$$

All V_z values have the same non-dimensional velocity, $V_Z^* = -2.945$, and V_b^* is related to V_b through

$$V_b^* = 2.945\frac{V_b}{|V_z|} . \tag{19}$$

Eqns. (16) and (17) can be solved for a range of f^* values to produce a curve of ε_e versus f^*, similar to that shown in Fig. 12(a) but in non-dimensional form. The only additional adjustable parameter is V_b^*. A set of 'master curves' can thus be created, one for each V_b^*, as shown in Figure 12(b) for 5 representative V_b^* values.

5 Conclusions

A NMR technique has been used to measure height-resolved velocity distributions, as well as 1-D granular temperature and packing fraction profiles, inside a granular bed fluidised by ultrasonic vibration. The velocity distributions were qualitatively similar to those from low-frequency fluidised beds: close-to-Maxwellian distributions at high altitude, with increasing levels of distortion in the positive-velocity tail as the base is approached. Granular temperature was observed to increase slightly with height, even though the 'viscous damping of pressure wave' mechanism for such an increase seems unfeasible with a vibration period much smaller than the collision mean free time. The main difference observed in these experiments, compared to previous ones using low-frequency vibration sources, is the strong variation of granular temperature

with vibration frequency. Classical energy flux boundary conditions have no such frequency sensitivity, depending instead on the root mean square base velocity. Measurement of the elastic properties of the grains, together with 1-D modelling of the grain-boundary interactions, suggests that the cause of this effect is a loss of energy transfer efficiency as the vibration period drops towards the grain-boundary contact time.

6 Acknowledgments

MDM, AJS and LFG wish to thank the EPRSC for funding under Platform Grant EP/F047991/1.

Figure captions

Figure 1. Typical vibration period for ultrasonic and conventional vibration sources, compared to typical values of mean free time for grain-grain collisions τ_E, and of the grain-wall contact time τ_c.

Figure 2. Cross-section through ultrasonic source.

Figure 3. Force deflection curves for a single grain compressed between two PEEK anvils. (a) High force range; (b) low force range with experimental curves (dashed lines) and best-fit Hertzian curves (solid lines) for 3 grains.

Figure 4. Experimental setup. LV: laser vibrometer; M: mirror to direct LV beam onto the vibrating waveguide; NMR: NMR spectrometer; US: ultrasound source.

Figure 5. Effect of base velocity on ultrasonically fluidized bed. Time-averaged signal $S(v_z,z)$ with $N_g = 40$ and $f = 11.1$ kHz, at three base velocities $V_b = 0.33$ m s^{-1} (a), 0.5 m s^{-1} (b) and 0.74 m s^{-1} (c). Horizontal and vertical axes represent v_z and z with units of m s^{-1} and mm, respectively. The strongest signal appears red, the weakest blue.

Figure 6. Experimental velocity probability density functions (PDFs) at heights of 4 mm (a), 8 mm (b), and 16 mm (c), (continuous lines) together with Maxwellian least-squares fits (dashed lines). $f = 11.1$ kHz, $N_g = 40$, $V_b = 0.74$ m s^{-1}.

Figure 7. Variation of (a) granular temperature T_z and (b) packing fraction η with height z for three values of base velocity. $f = 11.1$ kHz, $N_g = 40$.

Figure 8. Effect of base velocity (a) and number of grains (b) on density-weighted mean non-dimensional granular temperature. $f = 11.1$ kHz.

Figure 9. Effect of number of grains on ultrasonically fluidized bed. $S(v_z,z)$ with N_g = 20 (a), 40 (b) and 60 (c), $f = 11.1$ kHz, and peak base velocity $V_b = 0.74$ m s^{-1}.

Figure 10. Effect of frequency on ultrasonically fluidized bed. $S(v_z,z)$ with $N_g = 20$, $f =$ 11.1 kHz (a), 17.7 kHz (b) and 20.2 kHz (c), with peak base velocity $V_b = 0.74$ m s^{-1}.

Figure 11. Base and grain displacement – time plots from numerical simulations for three base frequencies $f = 5$ kHz (a), 15 kHz (b), 50 kHz (c). Incoming grain velocity $V_z = -0.2$ m s^{-1}; peak base velocity $V_b = 0.74$ m s^{-1}.

Figure 12. Mean effective coefficient of restitution (ε_e) for base-grain interactions versus base frequency for base velocity $V_b = 0.74$ m s^{-1}; true coefficient of restitution = 1. (a) Incoming grain speed = 0.2 m s^{-1}; error bars show standard deviation of ε_e over 16 phases of the vibration cycle. Vertical and horizontal lines indicate the range of frequencies (11.1 kHz and 20.2 kHz) from Fig. 10. (b) Variation of ε_e with non-dimensional frequency, f^*, for six values (indicated on curves) of non-dimensional base velocity, V_b^*.

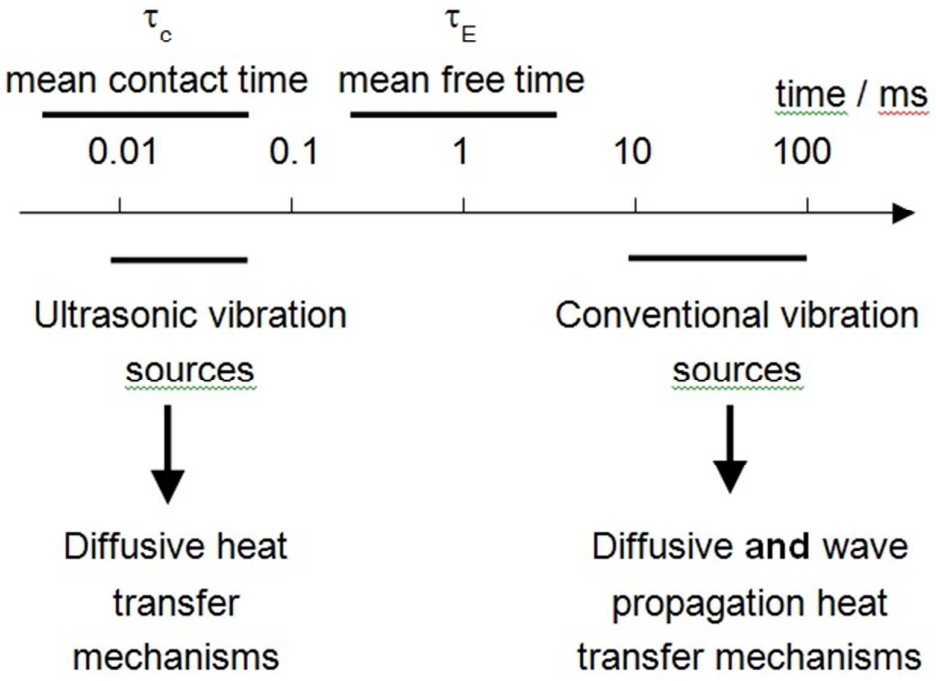

Figure 1.

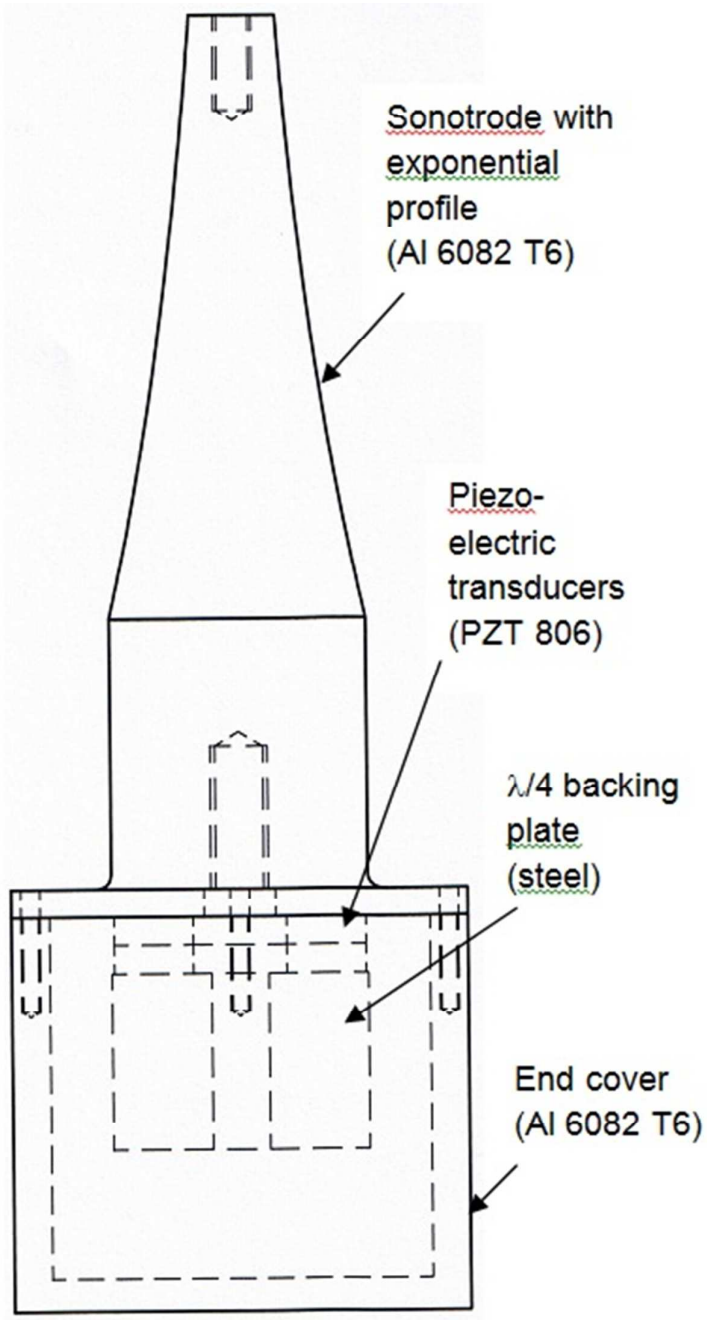
Sonotrode with exponential profile (Al 6082 T6)
Piezo-electric transducers (PZT 806)
λ/4 backing plate (steel)
End cover (Al 6082 T6)

Figure 2.

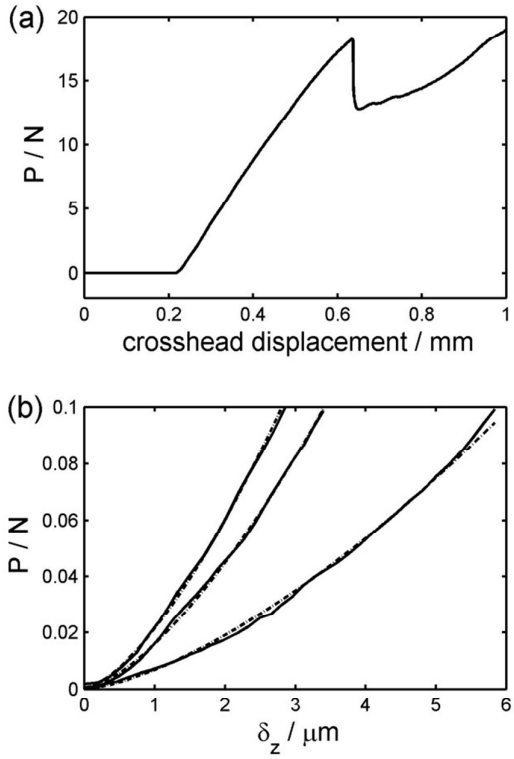

Figure 3.

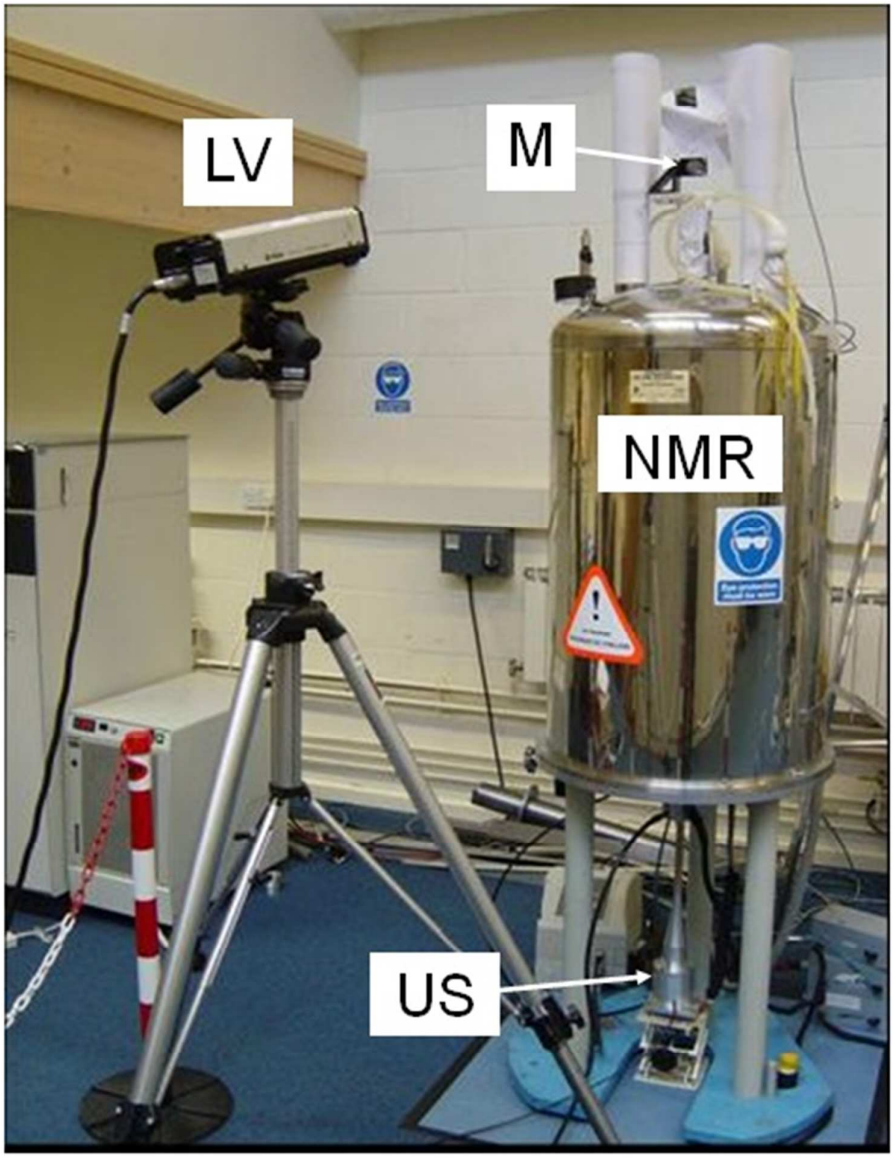

Figure 4.

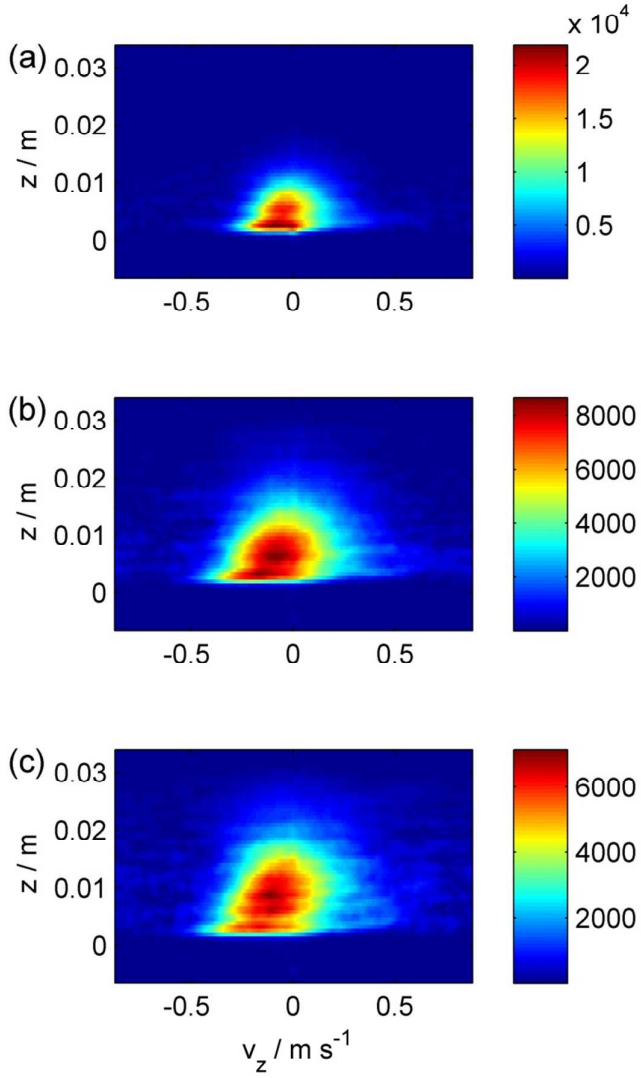
(a)
(b)
(c)
z / m
0.03
0.02
0.01
0
-0.5
0
0.5
x 10^4
2
1.5
1
0.5
8000
6000
4000
2000
v_z / m s^-1

Figure 5.

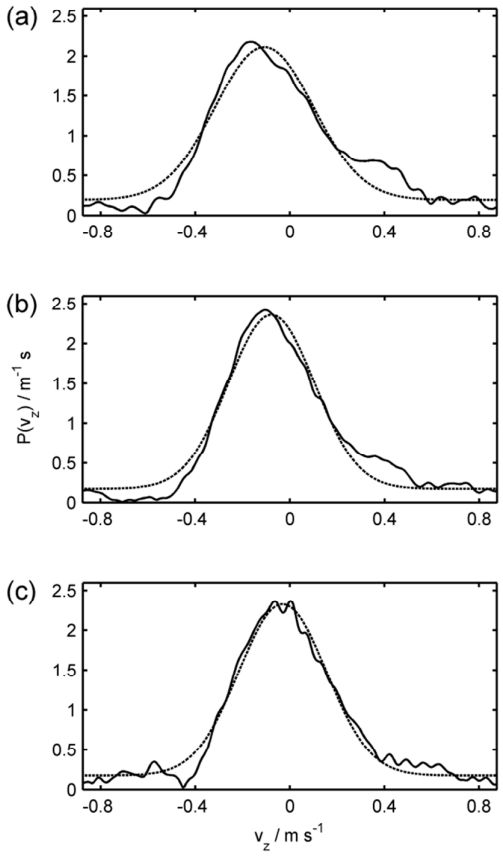

Figure 6.

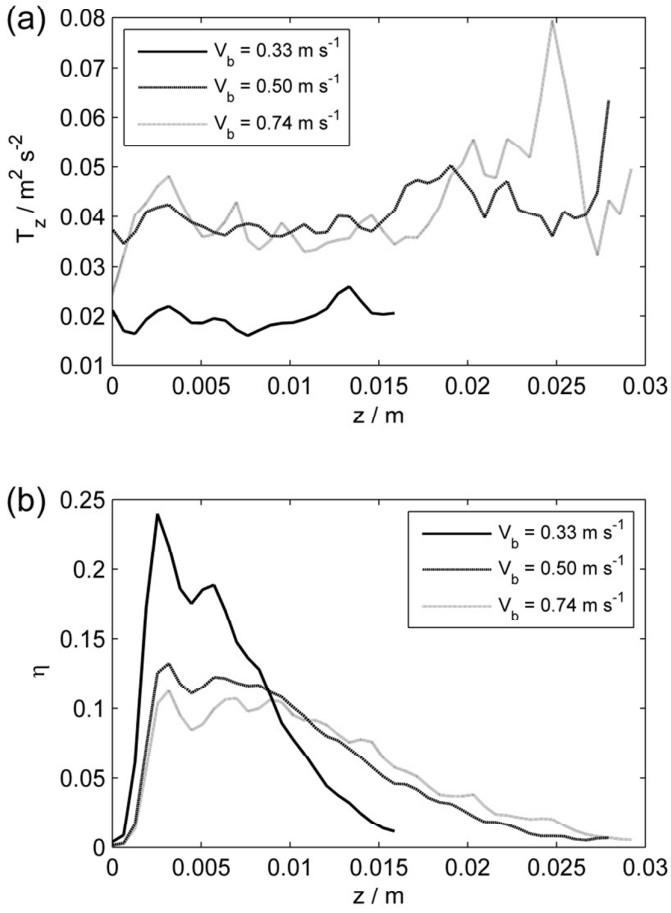
(a)
V_b = 0.33 m s^{-1}
V_b = 0.50 m s^{-1}
V_b = 0.74 m s^{-1}
T_z / m^2 s^{-2}
z / m
(b)
V_b = 0.33 m s^{-1}
V_b = 0.50 m s^{-1}
V_b = 0.74 m s^{-1}
η
z / m

Figure 7.

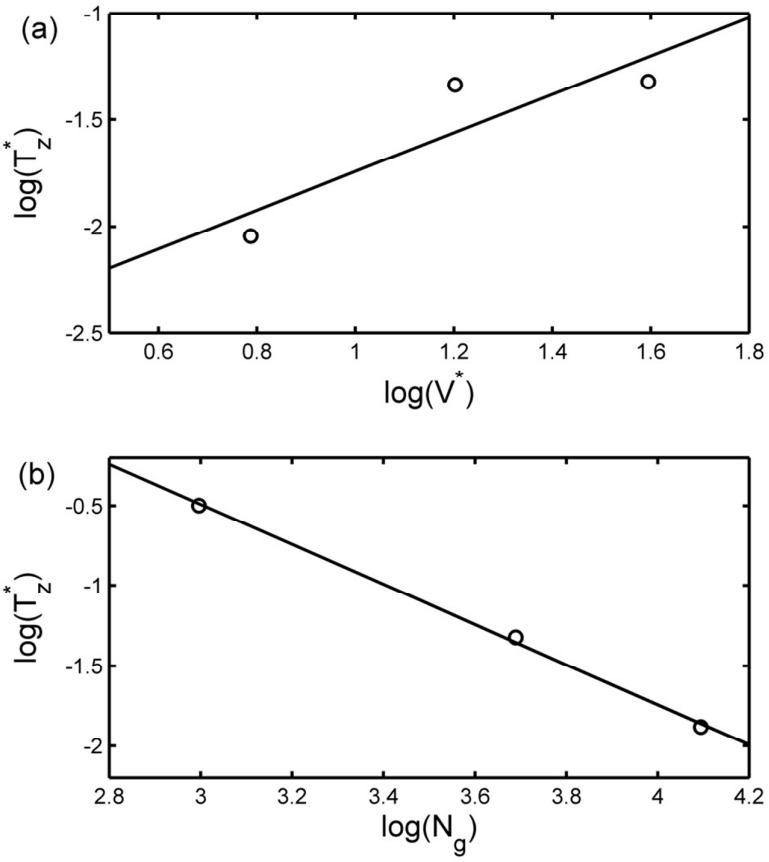

Figure 8.

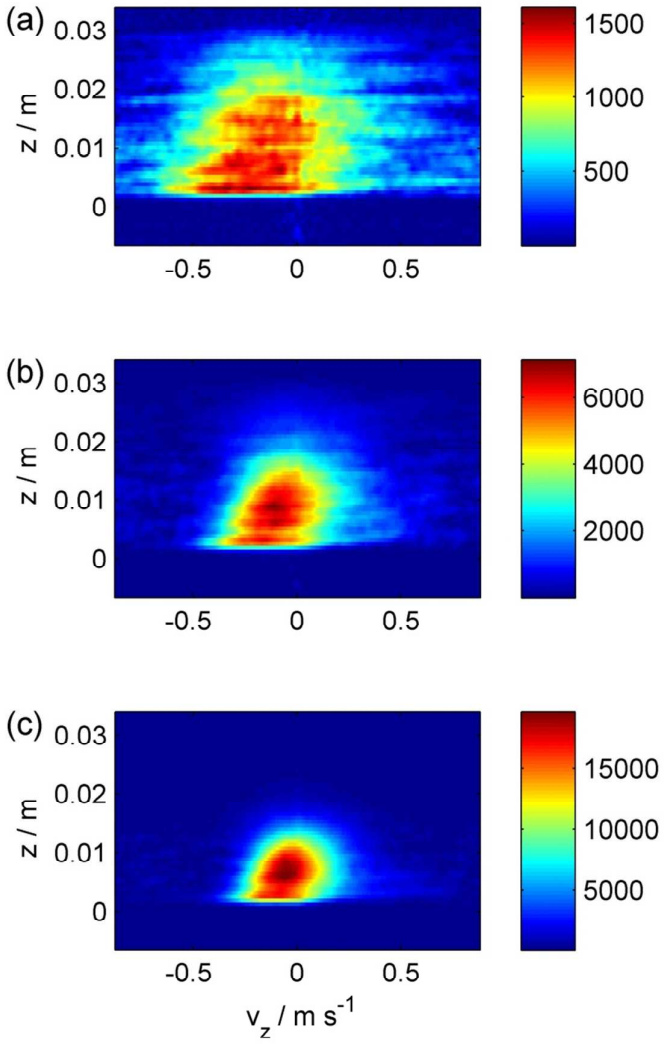
(a)
0.03
0.02
0.01
0
z / m
-0.5
0
0.5
1500
1000
500
(b)
0.03
0.02
0.01
0
z / m
-0.5
0
0.5
6000
4000
2000
(c)
0.03
0.02
0.01
0
z / m
-0.5
0
0.5
v_z / m s^{-1}
15000
10000
5000

Figure 9.

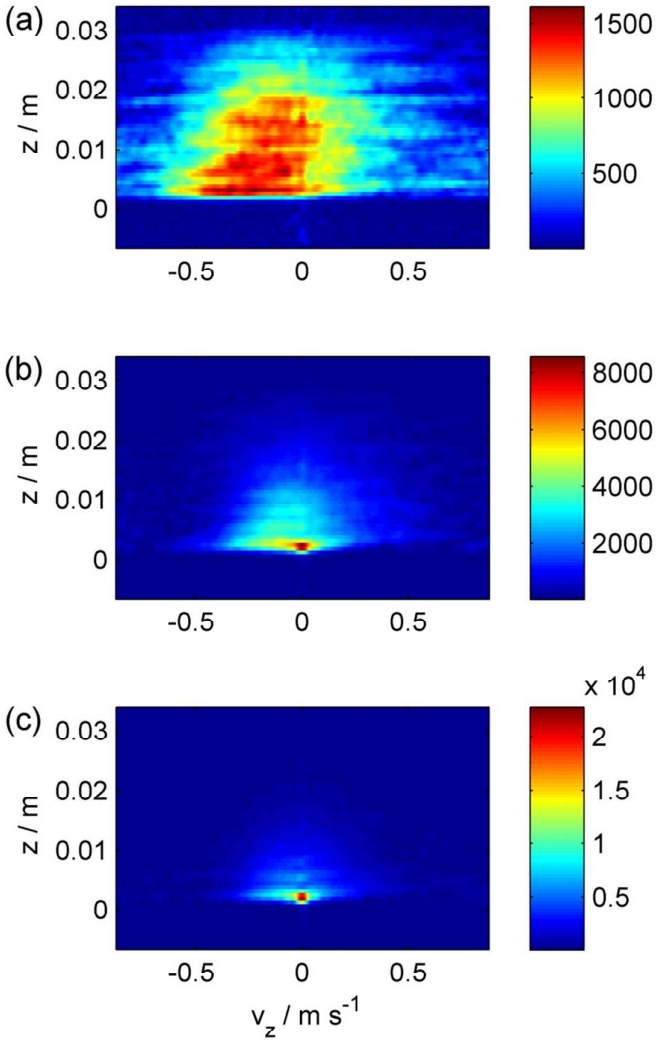
(a)
(b)
(c)
z / m
0.03
0.02
0.01
0
-0.5
0
0.5
1500
1000
500
8000
6000
4000
2000
x 10^4
2
1.5
1
0.5
v_z / m s^-1

Figure 10.

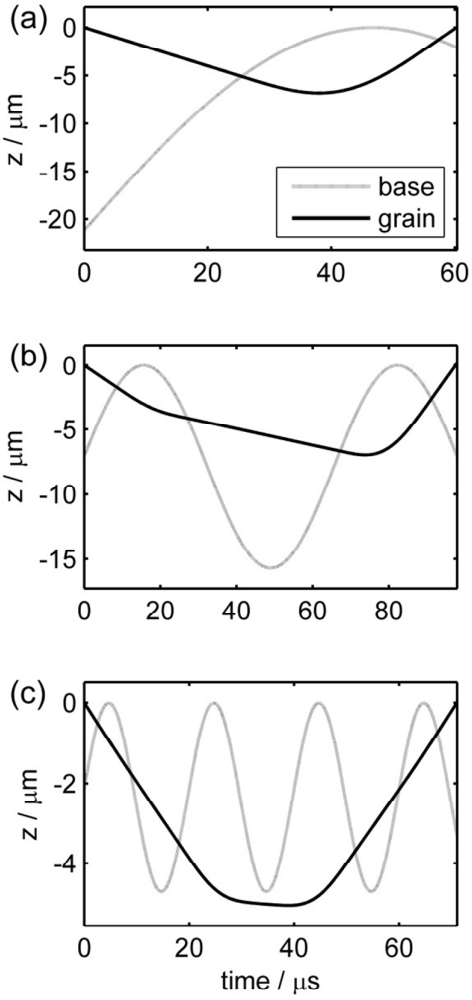
(a)
0
-5
-10
-15
-20
z / μm
base
grain
0
20
40
60
(b)
0
-5
-10
-15
z / μm
0
20
40
60
80
(c)
0
-2
-4
z / μm
0
20
40
60
time / μs

Figure 11.

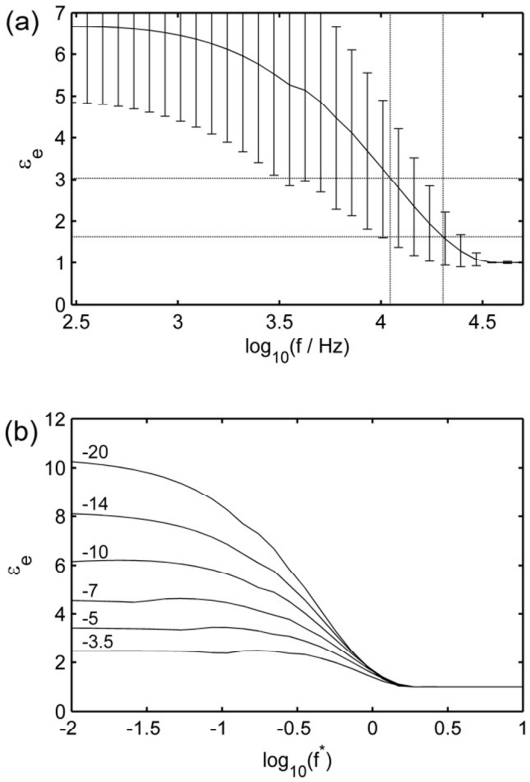

Figure 12.

7 References

1. Warr S, Hansen JP. Relaxation of local density fluctuations in a fluidized granular medium. Europhysics Letters. 1996;36(8):589-94.
2. Wildman RD, Huntley JM, Hansen JP. Self-diffusion of grains in a two-dimensional vibrofluidized bed. Phys Rev E. 1999;60(6):7066-75.
3. Wildman RD, Huntley JM, Parker DJ. Convection in highly fluidized three-dimensional granular beds. Phys Rev Lett. 2001;86(15):3304-7.
4. Jenkins JT, Richman MW. Kinetic-theory for plane flows of a dense gas of identical, rough, inelastic, circular disks. Physics of Fluids. 1985;28(12):3485-94.
5. Jenkins JT, Mancini F. Kinetic-theory for binary-mixtures of smooth, nearly elastic spheres. Physics of Fluids A-Fluid Dynamics. 1989;1(12):2050-7.
6. Wildman RD, Huntley JM, Parker DJ. Granular temperature profiles in three-dimensional vibrofluidized granular beds. Phys Rev E. 2001;6306(6):art. no.-061311.
7. Warr S, Huntley JM, Jacques GTH. Fluidization of a 2-dimensional granular system - experimental-study and scaling behavior. Phys Rev E. 1995;52(5):5583-95.
8. Huan C, Yang XY, Candela D, Mair RW, Walsworth RL. NMR experiments on a three-dimensional vibrofluidized granular medium. Phys Rev E. 2004;69(4):art. no.-041302.
9. Helal K, Biben T, Hansen JP. Local fluctuations in a fluidized granular medium. Physica A. 1997;240(1-2):361-73.
10. Ramirez R, Soto R. Temperature inversion in granular fluids under gravity. Physica A-Statistical Mechanics and its Applications. 2003;322(1-4):73-80.
11. Brey JJ, Ruiz-Montero MJ, Moreno F. Hydrodynamics of an open vibrated granular system. Phys Rev E. 2001;6306(6):art. no.-061305.
12. Sela N, Goldhirsch I. Hydrodynamic equations for rapid flows of smooth inelastic spheres, to Burnett order. Journal of Fluid Mechanics. 1998;361:41-74.
13. Brey JJ, Dufty JW, Kim CS, Santos A. Hydrodynamics for granular flow at low density. Phys Rev E. 1998;58(4):4638-53.
14. Soto R, Mareschal M, Risso D. Departure from Fourier's law for fluidized granular media. Phys Rev Lett. 1999;83(24):5003-6.
15. Barrat A, Trizac E, Ernst MH. Granular gases: dynamics and collective effects. Journal of Physics-Condensed Matter. 2005;17(24):S2429-S37.
16. Huntley JM, Martin TW, Mantle MD, Shattuck MD, Sederman AJ, Wildman RD, et al. NMR measurements and hydrodynamic simulations of phase-resolved velocity distributions within a three-dimensional vibrofluidized granular bed. Proceedings of the Royal Society a-Mathematical Physical and Engineering Sciences. 2007;463(2086):2519-42.
17. Crowder T, Hickey A. Powder specific active dispersion for generation of pharmaceutical aerosols. International Journal of Pharmaceutics. 2006;327(1-2):65-72.
18. Duchazeaubeneix JM. Stressonic Shot Peening (Ultrasonic Process). 7th International Conference on Shot Peening; 1999; Warsaw, Poland1999. p. 444-52.
19. Yang XY, Huan C, Candela D, Mair RW, Walsworth RL. Measurements of grain motion in a dense, three-dimensional granular fluid. Phys Rev Lett. 2002;88(4):art. no.-044301.
20. Frederick JR. Ultrasonic Engineering. New York: Wiley; 1965.
21. Johnson KL. Contact Mechanics. Cambridge: Cambridge University Press; 1985.

22. Mantle MD, Sederman AJ, Gladden LF, Huntley JM, Martin TW, Wildman RD, et al. MRI Investigations of Particle Motion within a Three-Dimensional Vibro-Fluidized Granular Bed. arXiv:cond-mat/0702201. 2007.
23. Pope JM, Yao S. Quantitative NMR imaging of flow. Concepts in Magnetic Resonance. 1993;5:281-302.
24. Luding S, Clement E, Blumen A, Rajchenbach J, Duran J. Studies Of Columns Of Beads Under External Vibrations. Phys Rev E. 1994;49(2):1634-46.
25. Richman MW. Boundary-conditions for granular flows at randomly fluctuating bumpy boundaries. Mech Mater. 1993;16(1-2):211-8.
26. Warr S, Huntley JM. Energy input and scaling laws for a single-particle vibrating in one-dimension. Phys Rev E. 1995;52(5):5596-601.
27. Chapra SCC, R. P. Numerical Methods for Engineers. 6th ed: McGraw-Hill; 2009.

NMR measurements of velocity distributions in an ultrasonically-vibrated granular bed

J M Huntley[1], T Tarvaz[1], M D Mantle[2], A J Sederman[2], L F Gladden[2], N A Sheikh[3], and R D Wildman[4]

1. Wolfson School of Mechanical and Manufacturing Engineering, Loughborough University, Loughborough LE11 3TU, UK
2. Department of Chemical Engineering, University of Cambridge, Pembroke Street, Cambridge CB2 3RA, UK
3. Muhammad Ali Jinnah University, Department of Mechanical Engineering, Islamabad, Pakistan
4. Department of Chemical and Environmental Engineering, University Park, Nottingham NG7 2RD, UK

Abstract We report the results of nuclear magnetic resonance (NMR) imaging experiments on granular beds of mustard grains fluidised by vertical vibration at ultrasonic frequencies. The variation of both granular temperature and packing fraction with height was measured within the three-dimensional cell for a range of vibration frequencies, amplitudes and numbers of grains. Small increases in vibration frequency were found – contrary to the predictions of classical 'hard-sphere' expressions for the energy flux through a vibrating boundary – to result in dramatic reductions in granular temperature. Numerical simulations of the grain-wall interactions, using experimentally-determined Hertzian contact stiffness coefficients, showed that energy flux drops significantly as the vibration period approaches the grain-wall contact time. The experiments thus demonstrate the need for new models for 'soft-sphere' boundary conditions at ultrasonic frequencies.

Keywords

Granular materials, rapid granular flow, vibrated granular bed, ultrasonic fluidisation, nuclear magnetic resonance, magnetic resonance imaging.

1 Introduction

Rapid flows of granular media occur frequently in nature (for example, avalanches and planetary ring formation) and in technology (for example, the transport of powders in the chemical and pharmaceutical industries). Improved understanding of devastating phenomena such as avalanches, and improved powder-based manufacturing techniques, requires a good understanding of the constitutive behaviour of granular materials in the inertial regime. Some striking similarities with the behaviour of a fluid in thermal equilibrium have been observed, e.g. in its microscopic structure [1], self-diffusion properties [2] and convection behaviour [3], despite the fact that dissipation due to collisions means a source of energy is required to sustain the motion and granular gases are therefore generally far from equilibrium. Theories have been developed relating variables such as packing fraction, granular temperature, shear rate, and heat flux for particular idealized situations such as monodisperse systems as well as some binary systems of hard spherical particles [4, 5].

However, there have been opposing views on the theoretical basis for some even relatively simple phenomena. For example, granular temperature would intuitively be expected to reduce with height above a vibrating base due to the inelastic grain-grain collisions, whereas in practice an upturn in granular temperature near the top of the bed has been observed both experimentally [6-8] and numerically [9-11]. One possible explanation [10, 11] arises from the predicted presence of a term in the Fourier heat law related to density gradient, in addition to the usual temperature gradient term [12-15]. An alternative explanation for the upturn, however, requires no

such density-gradient term but instead is based on viscous heating associated with compressional pressure waves induced by the moving boundary [16].

Experimental studies on vibrated granular gases have typically used a shaker operating at a few tens of Hz (see, for example, [7, 16]). In the current paper we investigate the effects of increasing the vibration frequency by some two to three orders of magnitude (to a few tens of kHz) through the use of high-power ultrasound technology. NMR measurements are used to probe the time-averaged and through-thickness-averaged distributions of velocity and packing fraction within the three-dimensional bed.

The motivation for this work is threefold. Firstly, the low frequency base of conventional vibrated granular beds acts not only as a means to fluidize the bed but also as a source of pressure waves which can add complexity to the interpretation of the experiments [16]. In the example cited above, it is not clear whether the density-gradient term in the Fourier law or the pressure waves are the main cause of the temperature upturn. In order to avoid this complication one requires a vibration period significantly shorter than the Enskog mean free time between collisions, τ_E. Figure 1 illustrates the point showing that this is indeed the case with ultrasound for typical experimental packing fractions and granular temperatures. As a result one is left with diffusion as the primary heat transfer mechanism and one may therefore expect ultrasound sources to act as a more idealized boundary than low-frequency ones, similar to the thermal boundaries sometimes used in simulations.

Secondly, with ultrasound, overlap may occur between the vibration period and the grain-boundary contact time τ_c as shown in Fig. 1. The latter typically ranges from a few μs to a few tens of μs depending on modulus, impact velocity and radius. The grain-boundary interactions may thus become sensitive to the constitutive and geometrical properties of the grains.

Finally, there are now several industrial applications of ultrasonically fluidised granular beds. In the pharmaceutical industry, inhalers have been developed in which ultrasound is used to fluidise a solid bed of dry powder [17]. In the case of shot peening, a process that introduces compressive residual stresses into metallic surfaces by repeated impacts with round particles, the particle motion can be sustained by impact with a second surface that is vibrating at frequencies of tens of kHz [18]. Improved knowledge of grain-boundary interactions at ultrasound frequencies therefore has the potential to optimise the performance of such processes.

The outline of the paper is as follows. The experimental set up, validation of the cell behaviour and mechanical compression tests to characterize the elastic properties of the grains are introduced in Section 2. Section 3 describes the results of the NMR experiments in which the main cell parameters (number of grains, base velocity and base frequency) are varied systematically. In Section 4, the results of numerical simulations to estimate the effective coefficient of restitution between a grain and vibrating base are presented as part of a wider discussion on the frequency dependence of the results from Section 4, before some concluding remarks in Section 5.

2 Experimental

2.1 Granular material

Most NMR experiments on granular materials use naturally occurring grains such as poppy or mustard seeds because the water or oil within them produce a strong NMR signal [16, 19]. For the present work, black mustard seeds were used on account of the relatively large diameter and narrow size range (diameter = 2.30 ± 0.20 mm). The mean grain mass, m, was 6.47 mg. Although not required elsewhere in the paper, the grain-boundary coefficients of restitution were measured using high speed photography as follows: mustard - PEEK 0.71 ± 0.03 mustard - PMMA 0.74 ± 0.02.

The values quoted represent the mean, and standard deviation in the mean, resulting from 10 impacts each.

2.2 Ultrasound source

The ultrasonic vibration source was designed in-house, based on well-established high-power ultrasonic engineering principles [20] and customised to the dimensions of the NMR spectrometer. Figure 2 shows a cross-section through the source. Two back-to-back lead zirconate titanate crystal rings (PZT 806, 54 mm diameter and with a 20 mm diameter central hole, manufactured by Morgan Electro Ceramics, UK), driven by a high voltage sinusoidal waveform, provide the acoustic energy. A steel backplate and aluminium cylinder above, each one quarter of a wave long at the designed resonant frequency of 20 kHz, provide a composite structure with the maximum displacement being produced at the top of the Al plate. An exponentially-tapered half-wavelength aluminium sonotrode then amplifies the motion further due to the reduction in cross-sectional area with height.

In order to transmit the ultrasonic energy from the end of the sonotrode into the measurement volume of the NMR spectrometer, it is necessary to use a waveguide. A set of 18-mm diameter cylindrical rods, manufactured from the polymer polyether ether ketone (PEEK) and joined by stainless steel studding, was used for this purpose. PEEK was chosen over metals such as aluminium to avoid distortions in the NMR signal, which can occur when conductors are near the measurement volume due to eddy-currents induced by the strong time-varying magnetic field gradients. Aluminium waveguides were also found to dissipate a significant fraction of the ultrasonic power when placed in the spectrometer, which is likely to be due to eddy currents induced in the aluminium rod by the travelling ultrasonic waves and the strong static magnetic field. The length of each section of the waveguide was made of an integral multiple of half the wavelength, giving a total waveguide length of 520 mm. The end of the last waveguide, with which the grains made contact, was

machined to a final diameter of 14 mm. The grains were contained within an open-ended cylindrical tube of internal diameter 14 mm made of PMMA supported on the outside of the waveguide with a rubber 'O' ring.

A laser vibrometer (Polytec OFV512 with OFV3001 controller) was used to monitor the surface velocity of the vibrating base. A peak velocity of 4 m s^{-1} was achievable at the design frequency of 20 kHz, although lower values than this were used in the experiments. Measurements were made every mm across the diameter of the cell base to test for uniformity of the vibration amplitude: the variation was found to be within the range ±2% for all the frequencies tested.

Figure 4 shows the experimental arrangement, with the ultrasonic source and waveguide positioned within the NMR spectrometer. The vibrometer beam was directed vertically downwards, through the open cell top, and onto the vibrating cell base by a mirror to allow in situ monitoring of the vibration amplitude.

2.3 Grain-boundary force-deflection curves

The simulations of the grain-base interactions described in Section 4 require an appropriate force-deflection model. The quasi-static mechanical response to diametral compression loading of a set of twelve grains was therefore measured using an Instron testing machine with 50 N load cell. Flat anvils were machined from PEEK to mimic the grain-base contact interactions during the ultrasonic fluidisation experiments.

Figure 3(a) shows a typical force-deflection curve for one of the tested grains. The response is approximately linear, up to a force of around 16 N at which point a sudden load drop indicates that grain fracture has occurred. At lower loads, however, the response is non-linear. Figure 3(b) shows the force (P) versus deflection (δ_z) curves over the range 0 to 0.1 N, together with the best-fit theoretical curve for a Hertzian contact,

$$P = K\delta_z^{3/2}, \tag{1}$$

for three of the grains (the first, 6th and 12th in order of increasing stiffness, K). Over this force range the average best-fit K value over the 12 grains was 1.47×10^7 N m$^{-3/2}$ with a standard deviation of 4.61×10^6 N m$^{-3/2}$. The δ_z values for the horizontal axis of Fig. 3(b) were calculated as one half of the crosshead displacement (to take account of the two contacts in a diametral compression test, as opposed to a single contact for the Hertzian theory) and a shift of the local origin to align it with the onset of loading.

In order to decide which force-deflection law is appropriate to the ultrasonically-fluidised granular medium, i.e. the high-load approximately-linear response of Fig. 3(a), or the low-load Hertzian response of Fig. 3(b), one needs to estimate the maximum contact force during a typical impact. Assuming that Hertzian impact theory is applicable [21], the maximum contact force P_m during an elastic impact for a grain with mass m and incoming velocity V_z is

$$P_m = K^{2/5}\left(\frac{5mV_z^2}{4}\right)^{3/5}. \qquad (2)$$

Substituting the values $K = 1.47\times10^7$ N m$^{-3/2}$, $m = 6.47$ mg, and a typical impact velocity V_z of 0.2 m s^{-1} results in a P_m value of 0.094 N. The force range shown in Fig. 3(b) is therefore applicable to the current situation, thus justifying the use of Eqn. 2 above and the subsequent analysis in Section 4.

2.4 NMR acquisition

A novel spin-echo velocity profiling technique was previously developed by the authors and described in Refs [22],[16]. This allows velocity distributions within a three-dimensional cell to be measured as a function of both vertical position (z) and phase of a low-frequency vibration. In the current study, the vibration frequency is too high to allow time-resolved measurements of velocity and temperature; the pulse sequence was therefore not triggered in any way.

The pulse sequence used in this study was that previously described in [22]. We chose here the vertical velocity component (v_z) since the granular temperature is normally

highest in this direction, although other components could be measured equally easily at the expense of additional acquisition time. The measured signal integrates through the thickness of the cell; in effect we traded spatial resolution in the horizontal directions (x or y) for the z and v_z resolution that are the primary focus of this paper. Previous studies on 2-D and 3-D vertically vibrated beds using high speed photography and PEPT [3, 7] have demonstrated that the main gradients in temperature and packing fraction occur along the z direction, with relatively minor perturbations in the horizontal directions.

All MRI experiments were acquired on a Bruker Biospin DMX 300 spectrometer operating at a ^{1}H frequency of 300.13 MHz. Spatial resolution was achieved using a three-orthogonal axis gradient system capable of producing a maximum gradient strength of 1 T m^{-1}. The field of view in the z-direction was 40.0 mm and the number of data points acquired was 128, thereby giving an axial pixel resolution of δz = 313 μm.

A 25 mm ^{1}H birdcage resonator was used to excite and detect the magnetisation from the mustard seeds and the ^{1}H 90 degree pulse length was 32 μs. The NMR pulse sequence of Mantle et al. [22] has two distinct advantages over a single-spin or stimulated-echo velocity profile sequence (used by, for example Huan et al. [8]): (i) it refocuses magnetisation dephasing due to constant motion in a linear background gradient [23]; (ii) the readout, or spatially encoding, gradients are also compensated for velocity artefacts. Ramped gradients were used throughout to minimise extra spin de-phasing from magnetic fields created by eddy currents due to gradient switching. The gradient ramp-up and ramp-down times were 100 μs. The total echo time TE was 2.14 ms. Velocity encoding was achieved by using 64 equal gradient increments from -0.8 T m^{-1} to +0.8 T m^{-1}.

The length of the velocity encoding gradient, δ, was 455 μs. The delay between velocity encoding gradient pulses, Δ, was 1.20 ms. Sixty four scans for each velocity

encoding increment, at a recycle time of 365 ms, were averaged to obtain a sufficient signal-to-noise ratio. Hence the total experimental time for a single vibration frequency was approximately 25 minutes. Following acquisition, the raw data was zero-filled to 256 data points in the velocity encode dimension, and then a 2-dimensional Fourier transform was applied to each set of data to give spatially encoded velocity profiles, denoted here by $S(v_z,z)$. These parameters enable the determination of velocities within a range –0.875 m s^{-1} to + 0.875 m s^{-1}, with a resolution of 0.007 m s^{-1}.

3 Experimental results

Three groups of experiments were carried out. In the first, the number of grains, N_g, and frequency of the ultrasound, f, were fixed whilst the peak base velocity, V_b, was varied. In the second, N_g was varied whilst the other parameters remained fixed. Finally, in the third group, the ultrasound frequency was varied together with the displacement amplitude so as to maintain a constant peak base velocity. This was possible because although the ultrasound source was designed for a fixed frequency, it was found to have significant resonances at other frequencies.

3.1 Effect of varying the base velocity

Three different base velocities were used: V_b = 0.33, 0.50 and 0.74 m s^{-1}. Figure 5 shows the measured time-averaged raw signal $S(v_z,z)$ for each with N_g = 40 and f = 11.1 kHz. Within each image the central 'blob' is the signal from the mustard grains, and the vertical and horizontal axes represent respectively z (height above the base) and v_z (the vertical velocity component). As this signal represents the output from a 2D Fourier transform without scaling or normalisation, the units for the signal in Figure 5 and other similar figures are arbitrary.

A slice through an image at a given height provides a signal proportional to the probability density function (PDF) for v_z at that height. Figure 6 shows three examples

of such PDFs from Fig. 5(c) at heights z = 4, 8 and 16 mm. Superimposed on the experimental PDFs are Maxwellian distributions produced by fitting the curves defined by

$$S_f(v_z, z) = \frac{C_1}{\sqrt{2\pi}\sigma} \exp\left(-\frac{\left(v_z - \langle v_z \rangle\right)^2}{2\sigma^2} \right) + C_2 , \quad (3)$$

to $S(v_z,z)$ on a row by row basis. The parameters C_1 (the peak amplitude), C_2 (the average signal offset due for example to background noise), σ (the peak width) and $\langle v_z \rangle$ (the velocity offset) are in general functions of z. The closest match between the experimental and best-fit curves is at high altitudes; this is to be expected because distortions to the PDF due to interaction with the base have been largely randomized through intergrain collisions. As the altitude is reduced, progressively larger deviations are seen, notably the appearance of a 'shoulder' centred around v_z = +0.4 m s^{-1} in Figure 6(a). Such distortions were also noted in previous low-frequency experiments [16] and were explained as being due to the energetic particles that had just left the base in the $+v_z$ direction.

Profiles of the z-component of the granular temperature, and the packing fraction, may be estimated from the best-fit parameters as

$$T_z(z) = \sigma^2(z) , \quad (4)$$

and

$$\eta(z) = \frac{N_g d^3}{6R^2} \frac{C_1(z)}{\int_0^\infty C_1(z) dz} , \quad (5)$$

respectively, where d is the grain diameter and R the radius of the cell [16]. These profiles are shown in Fig. 7 for the three datasets from Fig. 5. The temperature profiles show only a weak dependence on height. There is a hint of an upturn in the two highest velocity profiles at high z, although this is the region where the

uncertainty is greatest due to the lower signal levels. The packing fraction profiles are qualitatively consistent with previous studies (e.g. [6, 7, 16]), with a rapid increase to the maximum density a short distance above the base, and then an approximately exponential decay with z at higher altitudes.

A simple scaling relation to model the change in mean temperature of the bed with V_b and N_g was proposed in the 1990s as follows [7, 24]:

$$T \propto \frac{V_b^{\alpha}}{N_g^{\beta}}, \tag{6}$$

where $V_b = A_0\omega$, with A_0 the displacement amplitude of the vibration and $\omega = 2\pi f$ its angular frequency, and α and β are two empirically-determined scaling exponents. Typical α values reported in the literature range from 1.2-1.9 and β values from 0.3 to 0.8 [6].

A density-weighted average temperature was calculated from the temperature and packing fraction profiles and then plotted on logarithmic axes in Fig. 8(a), in non-dimensional form, to allow an estimate of the scaling exponent α to be obtained for the ultrasonically-vibrated bed. Non-dimensional temperature T_z^* is defined as follows:

$$T_z^* = T_z / gd. \tag{7}$$

The best-fit value for α of 0.90 is somewhat lower than previously reported values from the literature at low frequency, however the small number of data points plus the scatter about the best-fit line mean there is significant uncertainty in this parameter.

3.2 Effect of varying the number of grains

Three experiments were carried out with the values N_g = 20, 40 and 60, the other main parameters being held constant (f = 11.1 kHz, and V_b = 0.74 m s^{-1}). Figure 9 shows the resulting signal $S(v_z,z)$ for the three cases. As more grains are added, both the height

of the bed and the width of the velocity distribution are reduced. This can be understood qualitatively as a consequence of the increased number of dissipative grain-grain collisions that occur, on average, between the energy-injecting grain-base collisions. The density-weighted average temperature, calculated as described in the previous section, is plotted in Fig. 8(b) as a function of N_g. The straight line fit corresponds to a scaling exponent $\beta = 1.25$.

3.3 Effect of varying the frequency of the base

The ultrasonic source had a resonance at 20.2 kHz, close to the design frequency of 20 kHz, but also at several additional frequencies including 11.1 and 17.7 kHz. A_0 was varied so as to keep V_b constant at 0.74 m s^{-1} for all three experiments. According to classical energy flux boundary conditions (see for example [25]), the key parameter associated with the motion of the boundary is its root mean square velocity. All three experiments should therefore have resulted in the same level of fluidisation, if such classical formulae are applicable at ultrasonic frequencies.

It is clear from the results, however, presented as $S(v_z,z)$ in Figure 10(a)-(c), that there is a dramatic reduction in the granular temperature of the bed as f is increased from 11.1 kHz to 20.2 kHz. A possible explanation for this phenomenon is that at ultrasonic frequencies the period of vibration $T = 1/f$ may become comparable to the contact time, τ_c, whereas in the derivation of the boundary conditions it is implicitly assumed that τ_c is sufficiently small to be neglected. The overlap between T and typical τ_c values is illustrated in Fig. 1 with the other relevant timescales.

The duration of an elastic collision for a particle with incoming velocity V_z is given by

$$\tau_c = 2.87\left(\frac{m^2}{rE^{*2}|V_z|}\right)^{1/5} \tag{8}$$

where

$$\frac{1}{E^*} = \frac{1-\nu_1^2}{E_1} + \frac{1-\nu_2^2}{E_2} \quad . \tag{9}$$

and r is the radius of the grain. Variables E and ν represent Young's modulus and Poisson's ratio, respectively, with subscripts 1 and 2 referring to the grain and the boundary. In order to estimate τ_c for the current situation we therefore require a value for E^*. The results of the experiments in Section 2.3 provide this information because E^* is related to the measured Hertzian stiffness coefficient, K, as follows:[21]

$$K = \frac{4}{3} r^{1/2} E^* \quad . \tag{10}$$

Combining Eqns. (8) and (10) with the value $K = 1.47\times10^7$ N m$^{-3/2}$, and a typical impact velocity V_z of -0.2 m s^{-1} results in a τ_c value of 51 μs. This is indeed comparable to the period of 50-90 μs for the vibration frequency range of 11-20 kHz. For this reason, simulations have been carried out to estimate the frequency dependence of the average increase in speed of a grain due to a grain-boundary impact. The approach used and the results are summarised in the next section.

4 Numerical simulations of grain-boundary interactions

A full analysis of the granular temperature distribution within the bed is beyond the scope of the current paper; we focus instead on estimating the changes in average rebound velocity with frequency for a single impact. Analysis of a particle interacting with a base undergoing 'sawtooth' motion has been carried out by Warr *et al*. for the case of instantaneous collisions [26]. The finite-contact-time problem is much more difficult to solve analytically. A model was therefore developed in which the one-dimensional equation of motion for a particle approaching a vibrating base in the vertical direction is solved numerically.

Applying Newton's second law with the Hertzian force-displacement law (Eqn. (1)), and neglecting gravity for the duration of the impact, the position of the centre of mass of the grain, z_c, is given by the 2nd order nonlinear ordinary differential equation:

$$\frac{d^2 z_c}{dt^2} = \frac{K}{m}(z_b - z_c + r)^{3/2} H(z_b - z_c + r) \tag{11}$$

where z_b is the position of the base:

$$z_b = -A_0[\sin(\omega t + \phi) - 1], \tag{12}$$

t is time, ϕ is a phase offset and $H(z)$ is the Heaviside step function ($H(z) = 1$, $z \geq 0$; $H(z) = 0$, $z < 0$). No loss terms are included in Eqn. (11), so that in the absence of vibration ($A_0 \to 0$) the rebound speed equals the speed of approach, i.e. the coefficient of restitution $\varepsilon \to 1$.

Equation (11) can be simplified by the substitution of the variable $z = z_c - r$ as follows:

$$\frac{d^2 z}{dt^2} = \frac{K}{m}(z_b - z)^{3/2} H(z_b - z). \tag{13}$$

z can be thought of as the position of a particle of zero radius, which allows the grain and base trajectories to be plotted on the same axes.

Equation (13) may be redefined as two first order ordinary differential equations in the variables $z_1 = z$ and $z_2 = dz/dt$, which can then be solved using standard 4th order Runge-Kutta techniques [27]. The initial conditions are $z_1(0) = 0$, $z_2(0) = -V_z$, and a time step of $\tau_c/100$ was used for all the results presented here.

Typical impact trajectories are shown in Figure 11 for three different base frequencies, with an arbitrary phase offset $\phi = 0.1$. Repeated impacts are apparent in the two higher frequency cases before the grain passes back upwards through the position $z = 0$. Integration is terminated at this point, with the value of z_2 here allowing an effective coefficient of restitution to be calculated as

$$\varepsilon_e = -z_2^+(0)/z_2^-(0). \tag{14}$$

Superscripts + and – indicate the sign of z_2, and thus refer to the post- and pre-impact velocities, respectively.

ε_e is an indicator of the energy injected into the bed, with larger values expected to produce a higher level of fluidisation than smaller ones. We use this therefore as a measure of the effectiveness of the vibrating base at different frequencies whilst maintaining a constant peak base velocity $V_b = A_0\omega$.

The phase of the base relative to the time at which the particle passes downwards through $z = 0$ is essentially random because of the very large number of base cycles between successive base-grain impacts. Simulations were therefore done over 16 values of ϕ uniformly distributed over the range 0 to 2π. Figure 12(a) shows the average ε_e from the 16, with error bars indicating the standard deviation, for the case V_b = 0.74 m s^{-1}. Experimentally-determined values of K and m were used throughout.

At low frequencies, ε_e is seen to be independent of frequency, consistent with standard boundary conditions where V_b is the sole dynamic parameter controlling energy flux[25]. At very high frequencies, $\varepsilon_e \to 1$, the same value as for a stationary base. The intermediate region, where the vibration period is comparable to the impact duration, is where ε_e is changing most quickly with f. The two relevant frequencies, f = 11.1 and 20.2 kHz, have ε_e values of 3.04 and 1.63, respectively. The approximate halving of rebound velocity (and corresponding reduction in energy input by ~80%) thus provides a plausible explanation for the strong reduction in level of fluidisation between Fig. 10(a) and 10(c).

The reason for the strong reduction in ε_e as f approaches $1/\tau_c$ can be understood in qualitative terms as follows. For the case where f is small compared to $1/\tau_c$, the change in grain velocity from a single collision depends on the instantaneous velocity of the base: the grain gains energy when the base is moving up whereas it loses energy when the base is moving down. As shown in Ref. [26], a grain-base collision is statistically more likely to occur when the base is moving up which means that, on the average, a grain gains rather than loses energy from the base in this low-frequency regime. At $f = 1/\tau_c$, however, the interaction between base and grain lasts for one

complete cycle of the vibration. Thus, although the grain is gaining energy on the part of the cycle when the base is moving up, the base then extracts some of this energy from the grain during the other half of the cycle when the base is moving down. This mechanical averaging effect becomes progressively more effective at smoothing out the fluctuations in energy input to the grain (base moving up) and energy extracted from the grain (base moving down) as f increases further beyond $1/\tau_c$, so that eventually $\varepsilon_e \to 1$ as $f \to \infty$.

In order to generalise the results to other granular materials, base velocities and approach velocities, it is convenient to recast Eqns. (12) and (13) in non-dimensional form. Time and frequency are normalised using the contact time, τ_c, so that $t^* = t/\tau_c$ and $f^* = f\tau_c$, where superscript '*' is used to denote a non-dimensional variable. Displacements z and z_b, and amplitude A_0, are normalised using the maximum indentation depth, z_m, which occurs at the maximum contact force P_m during an elastic impact on a stationary base:

$$z_m = \left(\frac{5mV_z^2}{4K}\right)^{2/5}. \tag{15}$$

In non-dimensional form, Eqns. (13) and (12) then read respectively

$$\frac{d^2z^*}{dt^{*2}} = C(z_b^* - z^*)^{3/2}H(z_b^* - z^*) \tag{16}$$

and

$$z_b^* = -A_0^*[\sin(\omega^* t^* + \phi) - 1], \tag{17}$$

where $\omega^* = 2\pi f^*$, C = 10.84 and

$$A_0^* = V_b^*/\omega^* . \tag{18}$$

All V_z values have the same non-dimensional velocity, $V_Z^* = -2.945$, and V_b^* is related to V_b through

$$V_b^* = 2.945\frac{V_b}{|V_z|}. \tag{19}$$

Eqns. (16) and (17) can be solved for a range of f^* values to produce a curve of ε_e versus f^*, similar to that shown in Fig. 12(a) but in non-dimensional form. The only additional adjustable parameter is V_b^*. A set of 'master curves' can thus be created, one for each V_b^*, as shown in Figure 12(b) for 5 representative V_b^* values.

5 Conclusions

A NMR technique has been used to measure height-resolved velocity distributions, as well as 1-D granular temperature and packing fraction profiles, inside a granular bed fluidised by ultrasonic vibration. The velocity distributions were qualitatively similar to those from low-frequency fluidised beds: close-to-Maxwellian distributions at high altitude, with increasing levels of distortion in the positive-velocity tail as the base is approached. Granular temperature was observed to increase slightly with height, even though the 'viscous damping of pressure wave' mechanism for such an increase seems unfeasible with a vibration period much smaller than the collision mean free time. The main difference observed in these experiments, compared to previous ones using low-frequency vibration sources, is the strong variation of granular temperature with vibration frequency. Classical energy flux boundary conditions have no such frequency sensitivity, depending instead on the root mean square base velocity. Measurement of the elastic properties of the grains, together with 1-D modelling of the grain-boundary interactions, suggests that the cause of this effect is a loss of energy transfer efficiency as the vibration period drops towards the grain-boundary contact time.

6 Acknowledgments

MDM, AJS and LFG wish to thank the EPRSC for funding under Platform Grant EP/F047991/1.

7 Data accessibility

NMR datasets (Figures 5, 9, 10): Dryad: (doi to be inserted following acceptance of article).

Figure captions

Figure 1. Typical vibration period for ultrasonic and conventional vibration sources, compared to typical values of mean free time for grain-grain collisions τ_E, and of the grain-wall contact time τ_c.

Figure 2. Cross-section through ultrasonic source.

Figure 3. Force deflection curves for a single grain compressed between two PEEK anvils. (a) High force range; (b) low force range with experimental curves (dashed lines) and best-fit Hertzian curves (solid lines) for 3 grains.

Figure 4. Experimental setup. LV: laser vibrometer; M: mirror to direct LV beam onto the vibrating waveguide; NMR: NMR spectrometer; US: ultrasound source.

Figure 5. Effect of base velocity on ultrasonically fluidized bed. Time-averaged signal $S(v_z,z)$ with $N_g = 40$ and $f = 11.1$ kHz, at three base velocities $V_b = 0.33$ m s^{-1} (a), 0.5 m s^{-1} (b) and 0.74 m s^{-1} (c). Horizontal and vertical axes represent v_z and z with units of m s^{-1} and mm, respectively. The signal level is quantified (in arbitrary units) in the colour bar. (Online version in colour.)

Figure 6. Experimental velocity probability density functions (PDFs) at heights of 4 mm (a), 8 mm (b), and 16 mm (c), (continuous lines) together with Maxwellian least-squares fits (dashed lines). $f = 11.1$ kHz, $N_g = 40$, $V_b = 0.74$ m s^{-1}.

Figure 7. Variation of (a) granular temperature T_z and (b) packing fraction η with height z for three values of base velocity. $f = 11.1$ kHz, $N_g = 40$.

Figure 8. Effect of base velocity (a) and number of grains (b) on density-weighted mean non-dimensional granular temperature. $f = 11.1$ kHz.

Figure 9. Effect of number of grains on ultrasonically fluidized bed. $S(v_z,z)$ with N_g = 20 (a), 40 (b) and 60 (c), f = 11.1 kHz, and peak base velocity V_b = 0.74 m s^{-1}. (Online version in colour.)

Figure 10. Effect of frequency on ultrasonically fluidized bed. $S(v_z,z)$ with N_g = 20, f = 11.1 kHz (a), 17.7 kHz (b) and 20.2 kHz (c), with peak base velocity V_b = 0.74 m s^{-1}. (Online version in colour.)

Figure 11. Base and grain displacement – time plots from numerical simulations for three base frequencies f = 5 kHz (a), 15 kHz (b), 50 kHz (c). Incoming grain velocity V_z = -0.2 m s^{-1}; peak base velocity V_b = 0.74 m s^{-1}.

Figure 12. Mean effective coefficient of restitution (ε_e) for base-grain interactions versus base frequency for base velocity V_b = 0.74 m s^{-1}; true coefficient of restitution = 1. (a) Incoming grain speed = 0.2 m s^{-1}; error bars show standard deviation of ε_e over 16 phases of the vibration cycle. Vertical and horizontal lines indicate the range of frequencies (11.1 kHz and 20.2 kHz) from Fig. 10. (b) Variation of ε_e with non-dimensional frequency, f^*, for six values (indicated on curves) of non-dimensional base velocity, V_b^*.

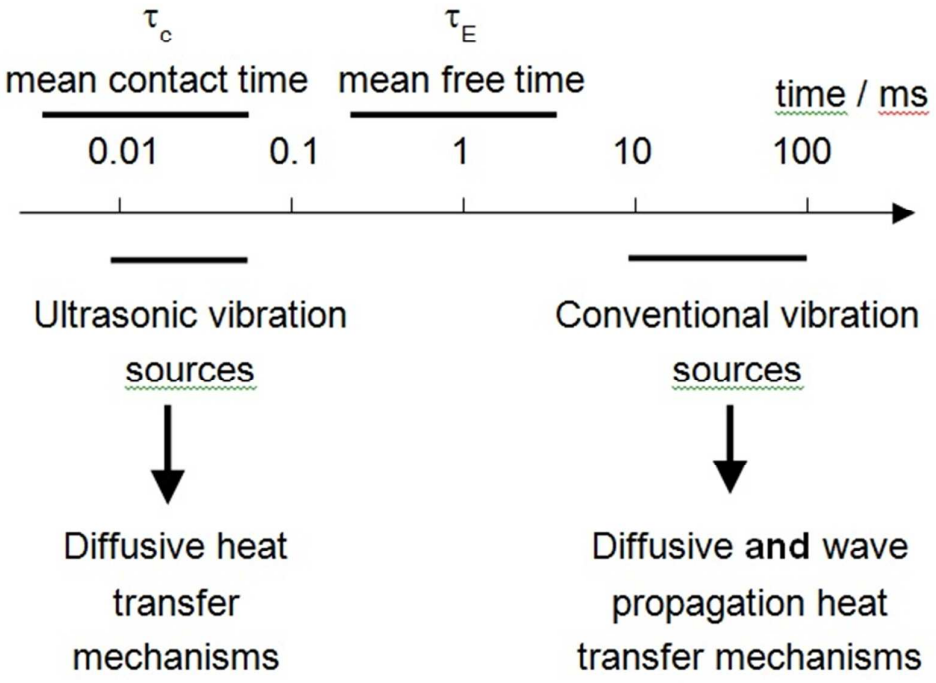

Figure 1.

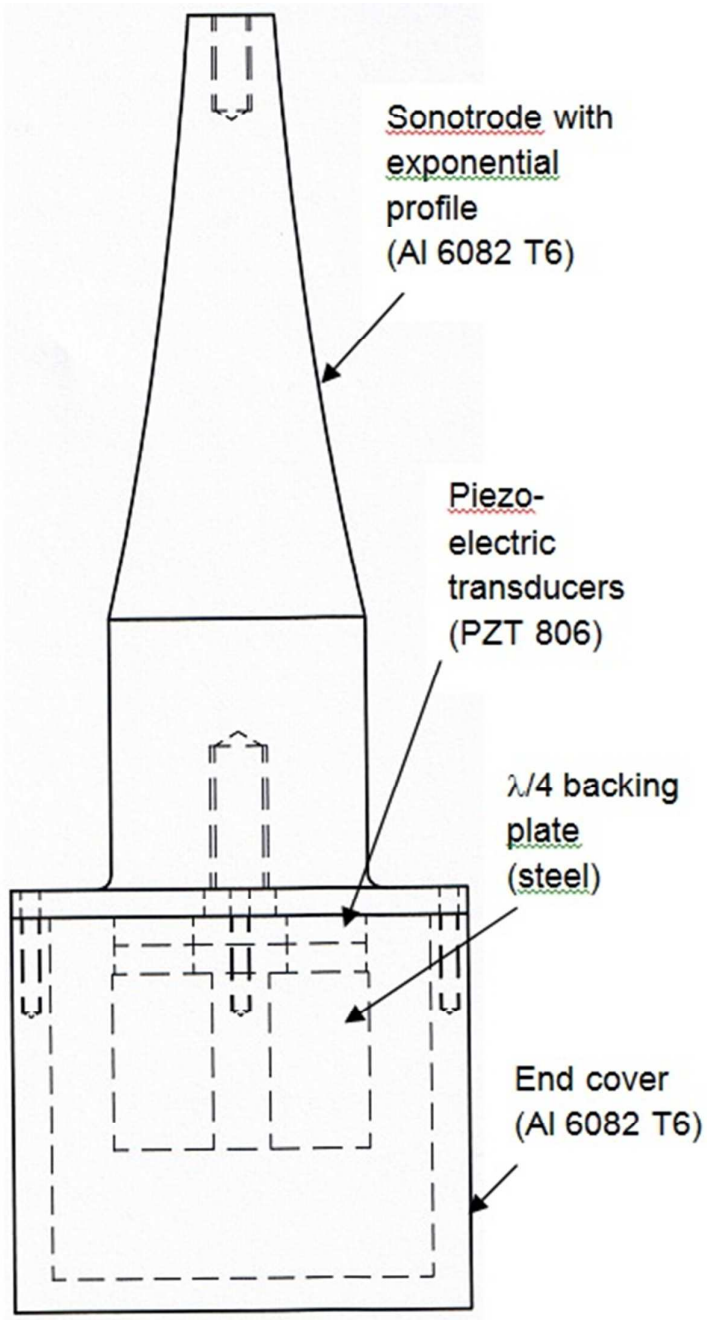
Sonotrode with exponential profile (Al 6082 T6)
Piezo-electric transducers (PZT 806)
λ/4 backing plate (steel)
End cover (Al 6082 T6)

Figure 2.

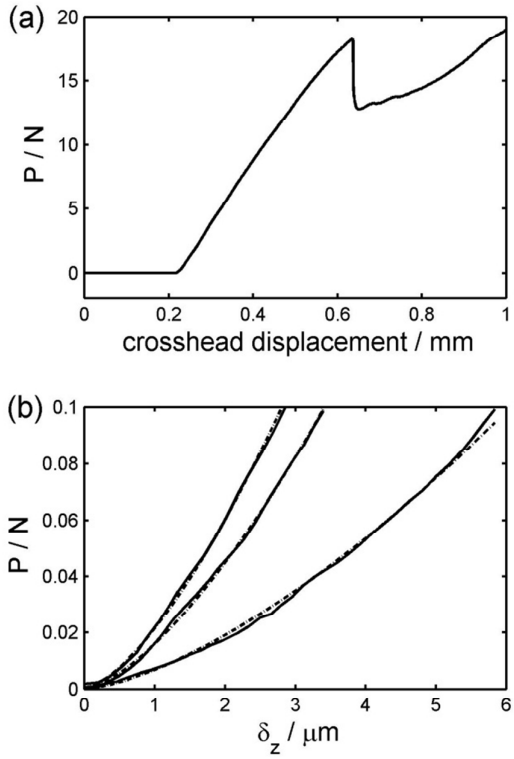

Figure 3.

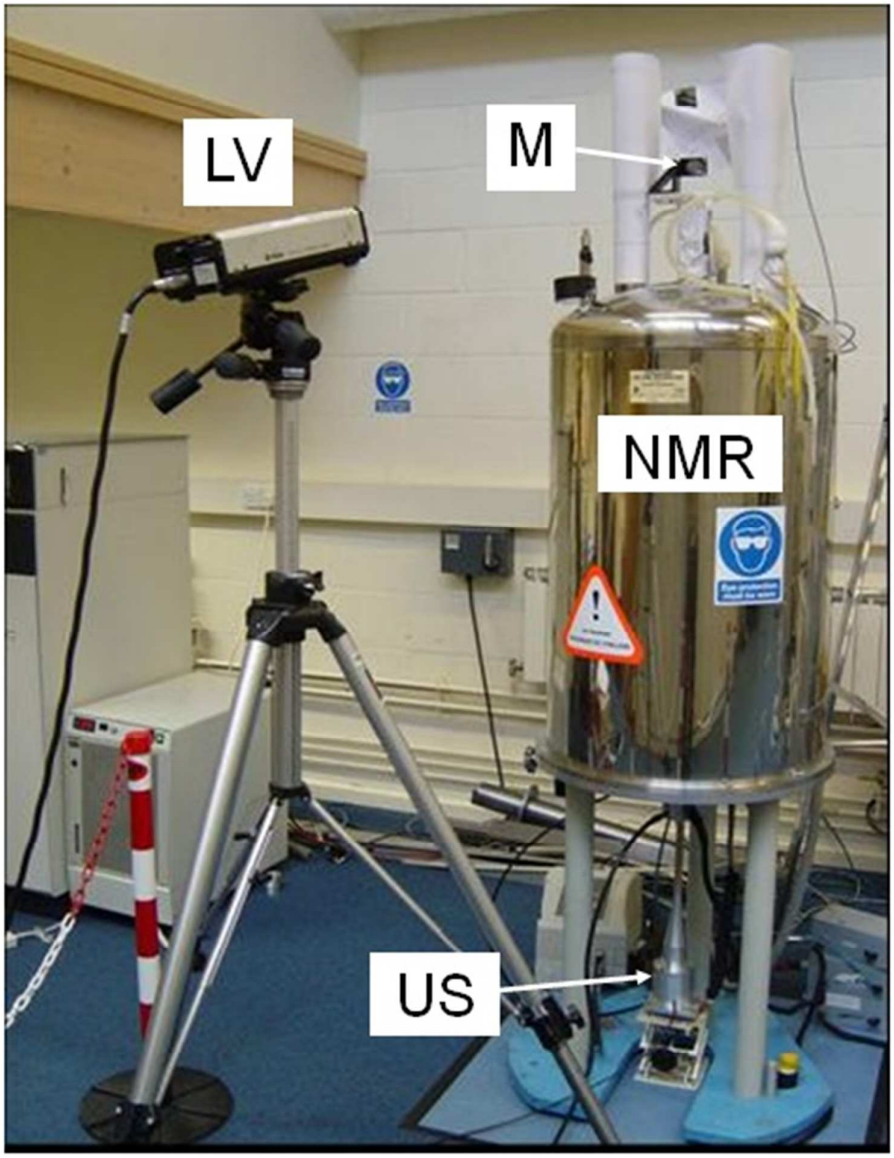

Figure 4.

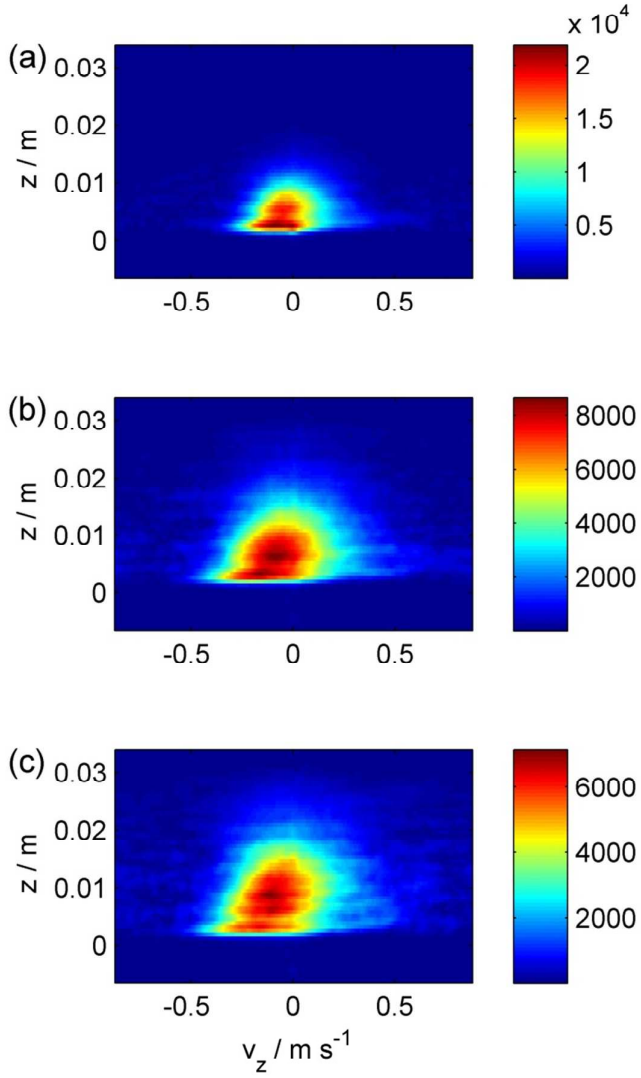
(a)
(b)
(c)
z / m
0.03
0.02
0.01
0
-0.5
0
0.5
x 10^4
2
1.5
1
0.5
8000
6000
4000
2000
v_z / m s^-1

Figure 5.

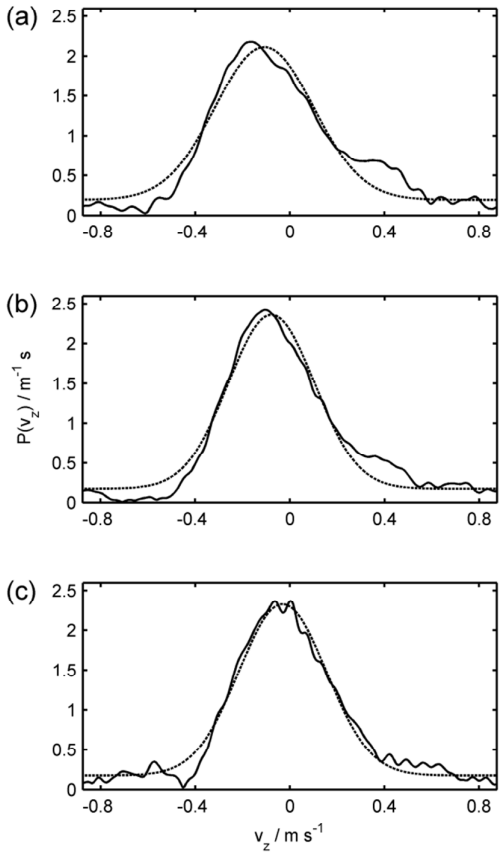

Figure 6.

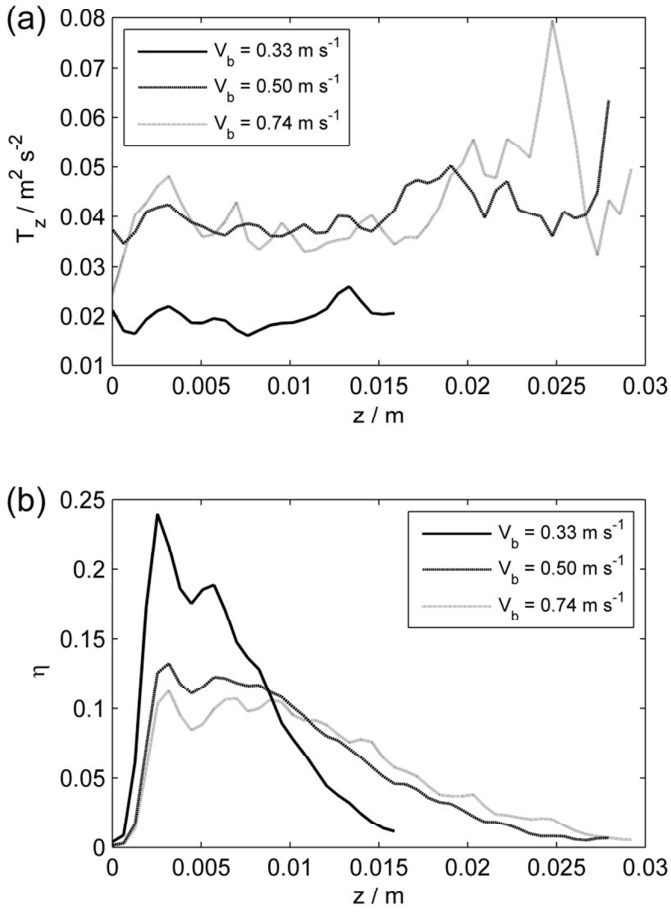
(a)
V_b = 0.33 m s^{-1}
V_b = 0.50 m s^{-1}
V_b = 0.74 m s^{-1}
T_z / m^2 s^{-2}
z / m
(b)
V_b = 0.33 m s^{-1}
V_b = 0.50 m s^{-1}
V_b = 0.74 m s^{-1}
η
z / m

Figure 7.

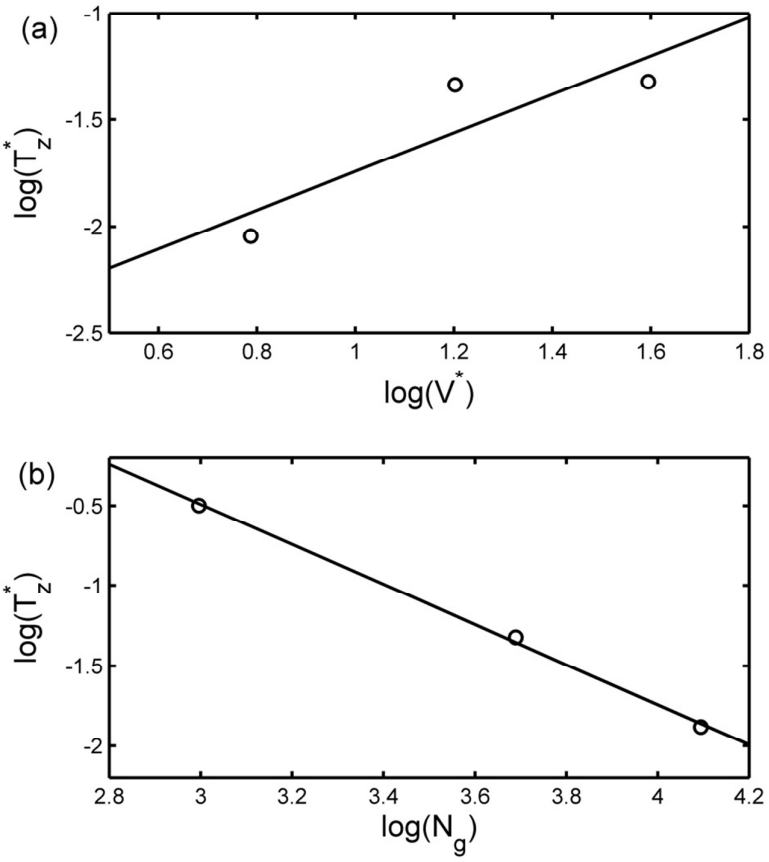
(a)
-1
-1.5
-2
-2.5
log(T*z)
0.6
0.8
1
1.2
1.4
1.6
1.8
log(V*)
(b)
-0.5
-1
-1.5
-2
log(T*z)
2.8
3
3.2
3.4
3.6
3.8
4
4.2
log(Ng)

Figure 8.

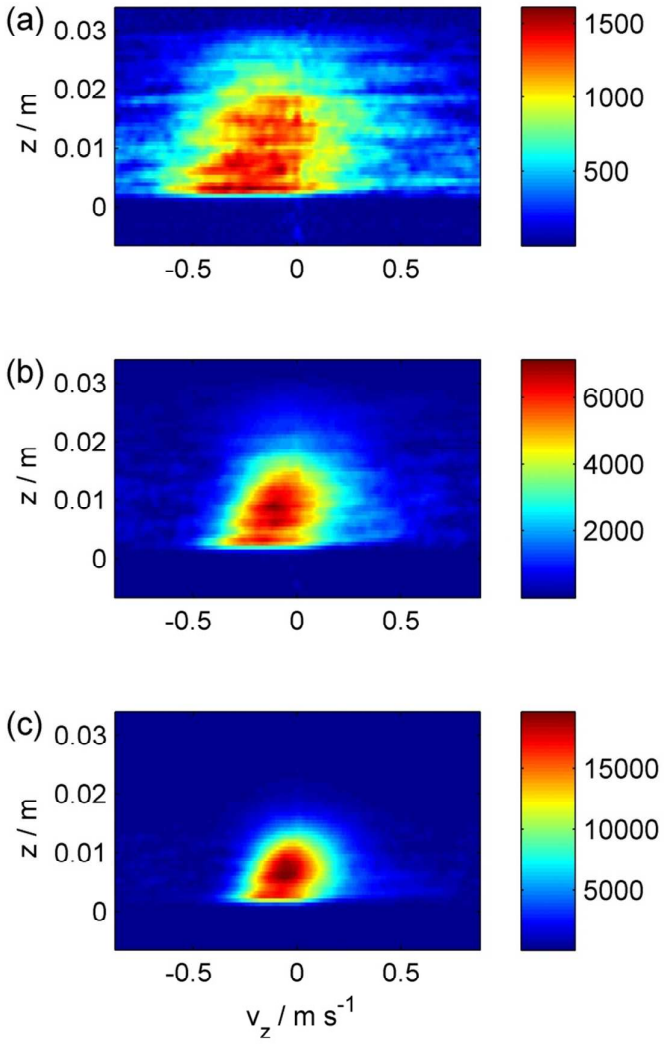
(a)
0.03
0.02
0.01
0
z / m
-0.5
0
0.5
1500
1000
500
(b)
0.03
0.02
0.01
0
z / m
-0.5
0
0.5
6000
4000
2000
(c)
0.03
0.02
0.01
0
z / m
-0.5
0
0.5
v_z / m s^{-1}
15000
10000
5000

Figure 9.

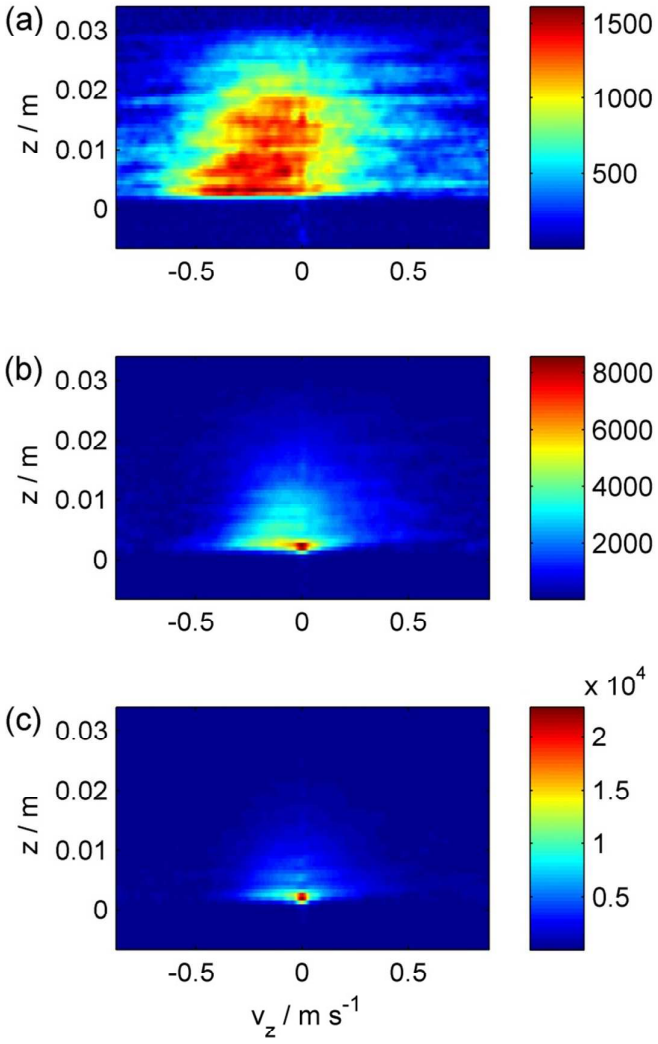
(a)
0.03
0.02
0.01
0
z / m
-0.5
0
0.5
1500
1000
500
(b)
0.03
0.02
0.01
0
z / m
-0.5
0
0.5
8000
6000
4000
2000
(c)
0.03
0.02
0.01
0
z / m
-0.5
0
0.5
v_z / m s^-1
x 10^4
2
1.5
1
0.5

Figure 10.

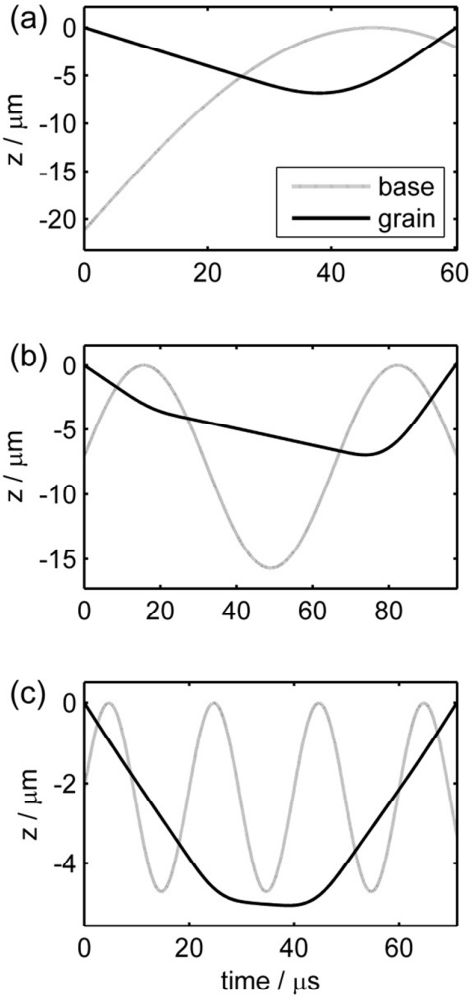
(a)
0
-5
-10
-15
-20
z / μm
base
grain
0
20
40
60
(b)
0
-5
-10
-15
z / μm
0
20
40
60
80
(c)
0
-2
-4
z / μm
0
20
40
60
time / μs

Figure 11.

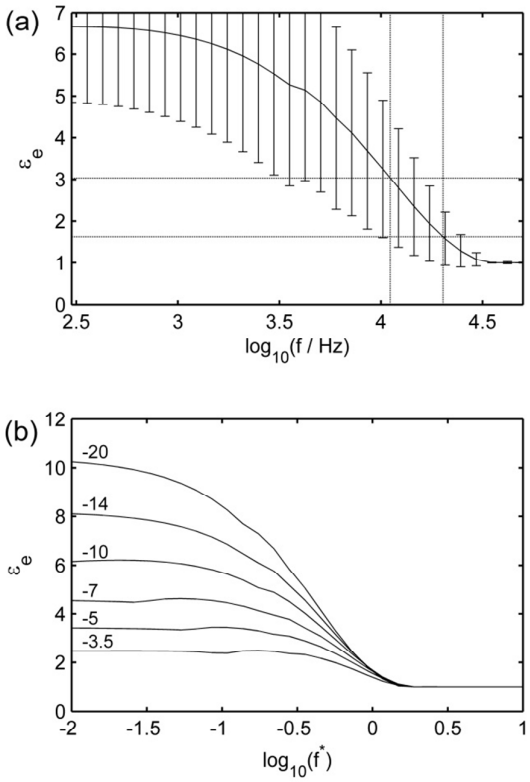

Figure 12.

8 References

[1] Warr, S. & Hansen, J.P. 1996 Relaxation of local density fluctuations in a fluidized granular medium. *Europhysics Letters* **36**, 589-594. (doi:10.1209/epl/i1996-00273-1).
[2] Wildman, R.D., Huntley, J.M. & Hansen, J.P. 1999 Self-diffusion of grains in a two-dimensional vibrofluidized bed. *Phys. Rev. E* **60**, 7066-7075. (doi:10.1103/PhysRevE.60.7066).
[3] Wildman, R.D., Huntley, J.M. & Parker, D.J. 2001 Convection in highly fluidized three-dimensional granular beds. *Phys. Rev. Lett.* **86**, 3304-3307. (doi:10.1103/PhysRevLett.86.3304).
[4] Jenkins, J.T. & Richman, M.W. 1985 Kinetic-theory for plane flows of a dense gas of identical, rough, inelastic, circular disks. *Physics of Fluids* **28**, 3485-3494. (doi:10.1063/1.865302).
[5] Jenkins, J.T. & Mancini, F. 1989 Kinetic-theory for binary-mixtures of smooth, nearly elastic spheres. *Physics of Fluids A-Fluid Dynamics* **1**, 2050-2057. (doi:10.1063/1.857479).
[6] Wildman, R.D., Huntley, J.M. & Parker, D.J. 2001 Granular temperature profiles in three-dimensional vibrofluidized granular beds. *Phys. Rev. E* **6306**, art. no.-061311. (doi:10.1103/PhysRevE.63.061311).
[7] Warr, S., Huntley, J.M. & Jacques, G.T.H. 1995 Fluidization of a 2-dimensional granular system - experimental-study and scaling behavior. *Phys. Rev. E* **52**, 5583-5595. (doi:10.1103/PhysRevE.52.5583).
[8] Huan, C., Yang, X.Y., Candela, D., Mair, R.W. & Walsworth, R.L. 2004 NMR experiments on a three-dimensional vibrofluidized granular medium. *Phys. Rev. E* **69**, art. no.-041302. (doi:10.1103/PhysRevE.69.041302).
[9] Helal, K., Biben, T. & Hansen, J.P. 1997 Local fluctuations in a fluidized granular medium. *Physica A* **240**, 361-373. (doi:10.1016/S0378-4371(97)00159-3).
[10] Ramirez, R. & Soto, R. 2003 Temperature inversion in granular fluids under gravity. *Physica A-Statistical Mechanics and its Applications* **322**, 73-80. (doi:10.1016/SO378-4371(03)00028-1).
[11] Brey, J.J., Ruiz-Montero, M.J. & Moreno, F. 2001 Hydrodynamics of an open vibrated granular system. *Phys. Rev. E* **6306**, art. no.-061305. (doi:10.1103/PhysRevE.63.061305).
[12] Sela, N. & Goldhirsch, I. 1998 Hydrodynamic equations for rapid flows of smooth inelastic spheres, to Burnett order. *Journal of Fluid Mechanics* **361**, 41-74. (doi:10.1017/S0022112098008660).
[13] Brey, J.J., Dufty, J.W., Kim, C.S. & Santos, A. 1998 Hydrodynamics for granular flow at low density. *Phys. Rev. E* **58**, 4638-4653. (doi:10.1103/PhysRevE.58.4638).
[14] Soto, R., Mareschal, M. & Risso, D. 1999 Departure from Fourier's law for fluidized granular media. *Phys. Rev. Lett.* **83**, 5003-5006. (doi:10.1103/PhysRevLett.83.5003).
[15] Barrat, A., Trizac, E. & Ernst, M.H. 2005 Granular gases: dynamics and collective effects. *Journal of Physics-Condensed Matter* **17**, S2429-S2437. (doi:10.1088/0953-8984/17/24/004).
[16] Huntley, J.M., Martin, T.W., Mantle, M.D., Shattuck, M.D., Sederman, A.J., Wildman, R.D., Gladden, L.F. & Halliwell, N.A. 2007 NMR measurements and hydrodynamic simulations of phase-resolved velocity distributions within a three-dimensional vibrofluidized granular bed. *Proceedings of the Royal Society A-*

Mathematical Physical and Engineering Sciences **463**, 2519-2542. (doi:10.1098/rspa.2007.1885).
[17] Crowder, T. & Hickey, A. 2006 Powder specific active dispersion for generation of pharmaceutical aerosols. *International Journal of Pharmaceutics* **327**, 65-72. (doi:10.1016/j.ijpharm.2006.07.050).
[18] Duchazeaubeneix, J.M. 1999 Stressonic Shot Peening (Ultrasonic Process). In *7th International Conference on Shot Peening* (pp. 444-452. Warsaw, Poland.
[19] Yang, X.Y., Huan, C., Candela, D., Mair, R.W. & Walsworth, R.L. 2002 Measurements of grain motion in a dense, three-dimensional granular fluid. *Phys. Rev. Lett.* **88**, art. no.-044301. (doi:10.1103/PhysRevLett.88.044301).
[20] Frederick, J.R. 1965 *Ultrasonic Engineering*. New York, Wiley.
[21] Johnson, K.L. 1985 *Contact Mechanics*. Cambridge, Cambridge University Press.
[22] Mantle, M.D., Sederman, A.J., Gladden, L.F., Huntley, J.M., Martin, T.W., Wildman, R.D. & Shattuck, M.D. 2007 MRI Investigations of particle motion within a three-dimensional vibro-fluidized granular bed. *Powder Technology* **179**, 164-169. (doi:10.1016/j.powtec.2007.06.020).
[23] Pope, J.M. & Yao, S. 1993 Quantitative NMR imaging of flow. *Concepts in Magnetic Resonance* **5**, 281-302. (doi:10.1002/cmr.1820050402).
[24] Luding, S., Clement, E., Blumen, A., Rajchenbach, J. & Duran, J. 1994 Studies of columns of beads under external vibrations. *Phys. Rev. E* **49**, 1634-1646. (doi:10.1103/PhysRevE.49.1634).
[25] Richman, M.W. 1993 Boundary-conditions for granular flows at randomly fluctuating bumpy boundaries. *Mech. Mater.* **16**, 211-218. (doi:10.1016/0167-6636(93)90045-S).
[26] Warr, S. & Huntley, J.M. 1995 Energy input and scaling laws for a single-particle vibrating in one-dimension. *Phys. Rev. E* **52**, 5596-5601. (doi:10.1103/PhysRevE.52.5596).
[27] Chapra, S.C.C., R. P. 2009 *Numerical Methods for Engineers*. 6th ed, McGraw-Hill.

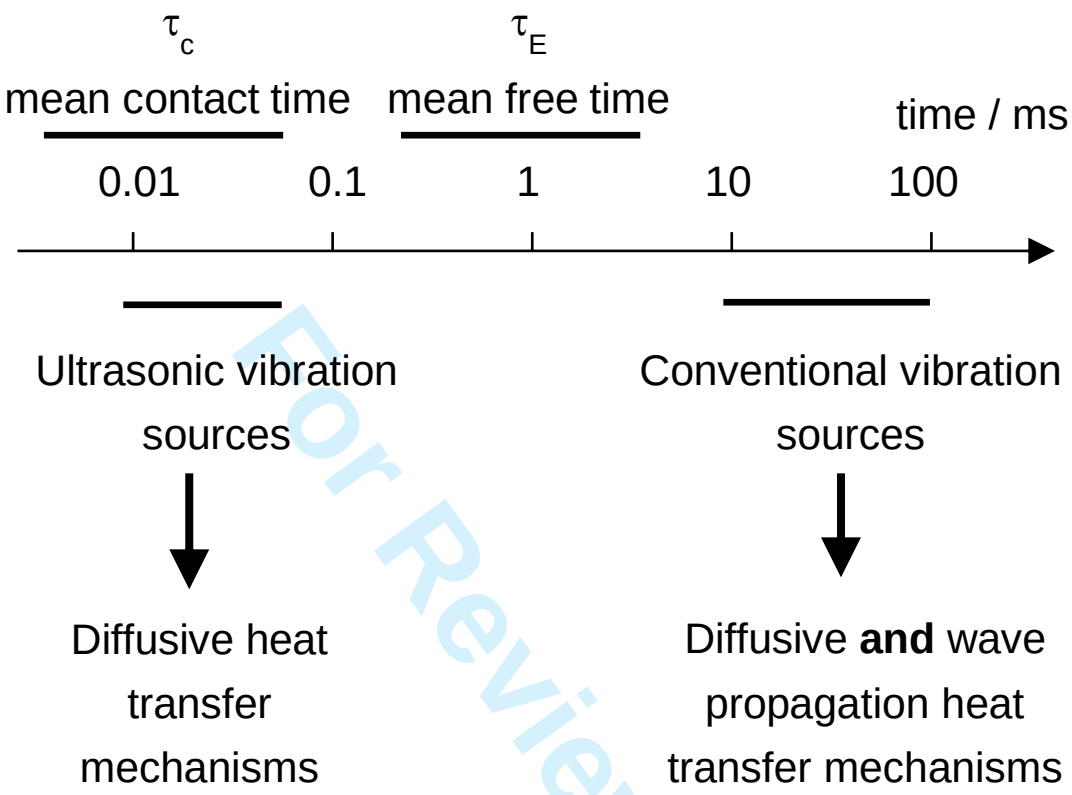

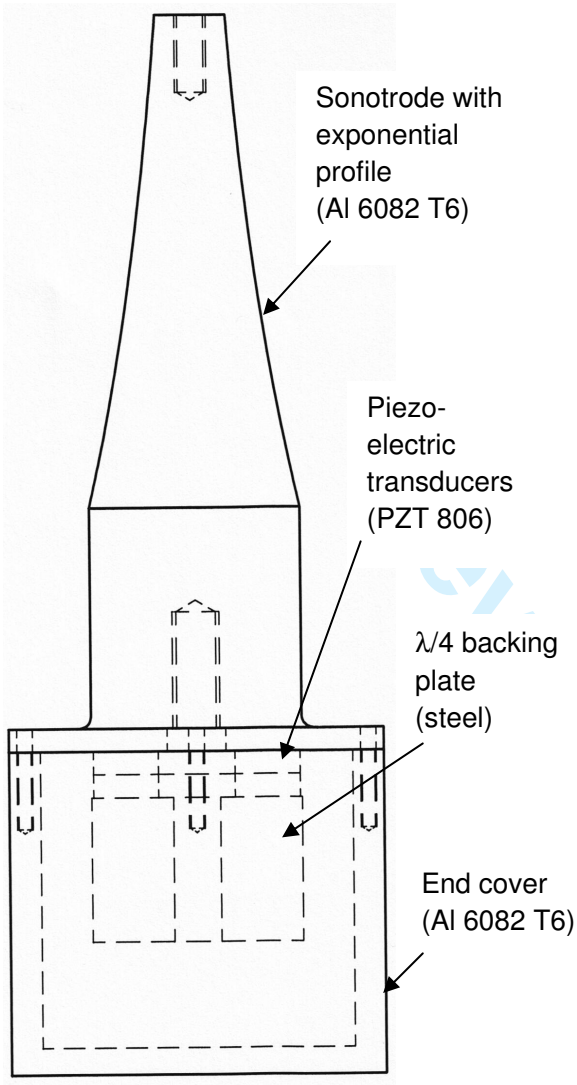

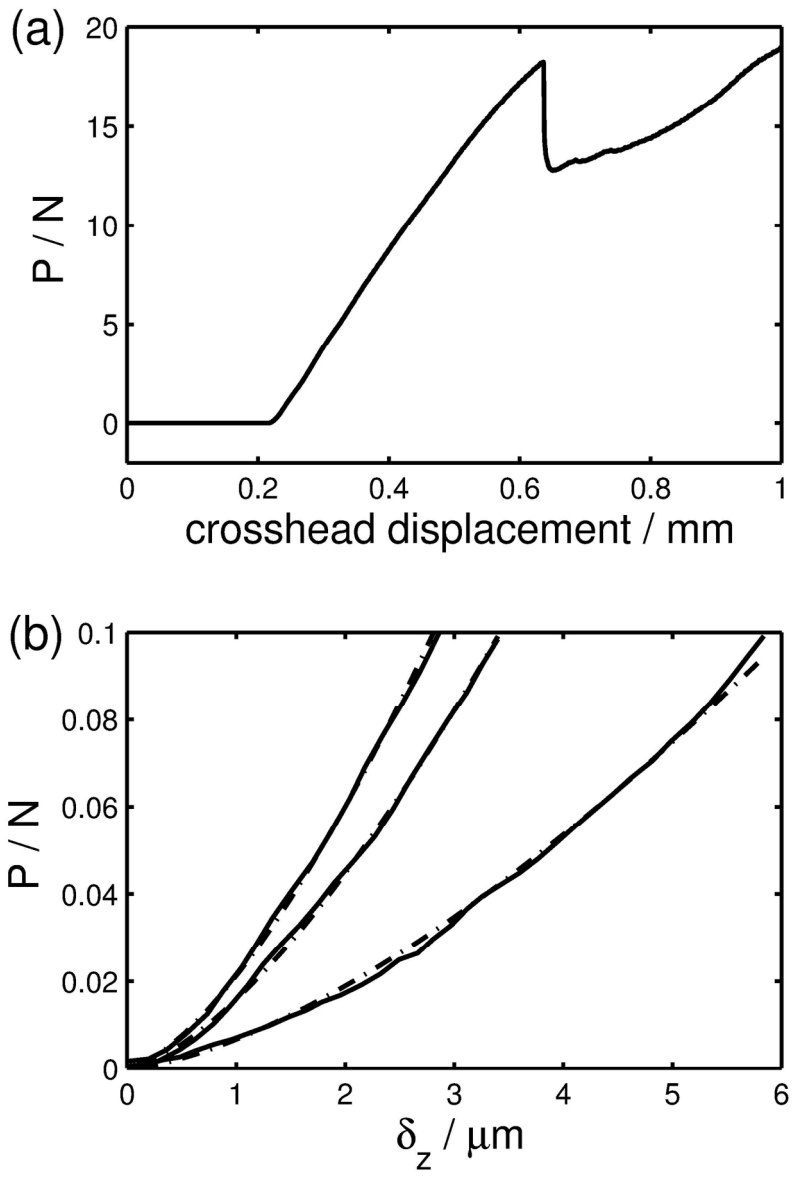

143x212mm (300 x 300 DPI)

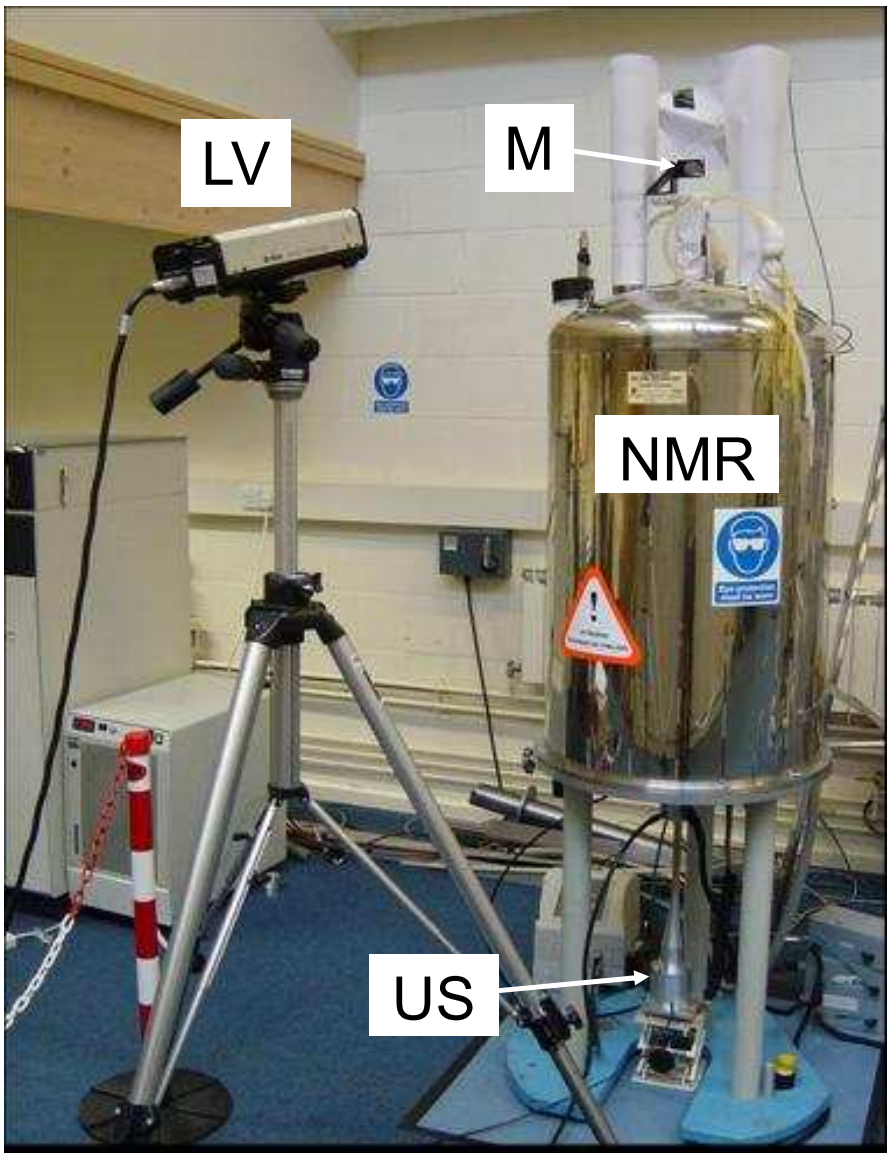
LV
M
NMR
US

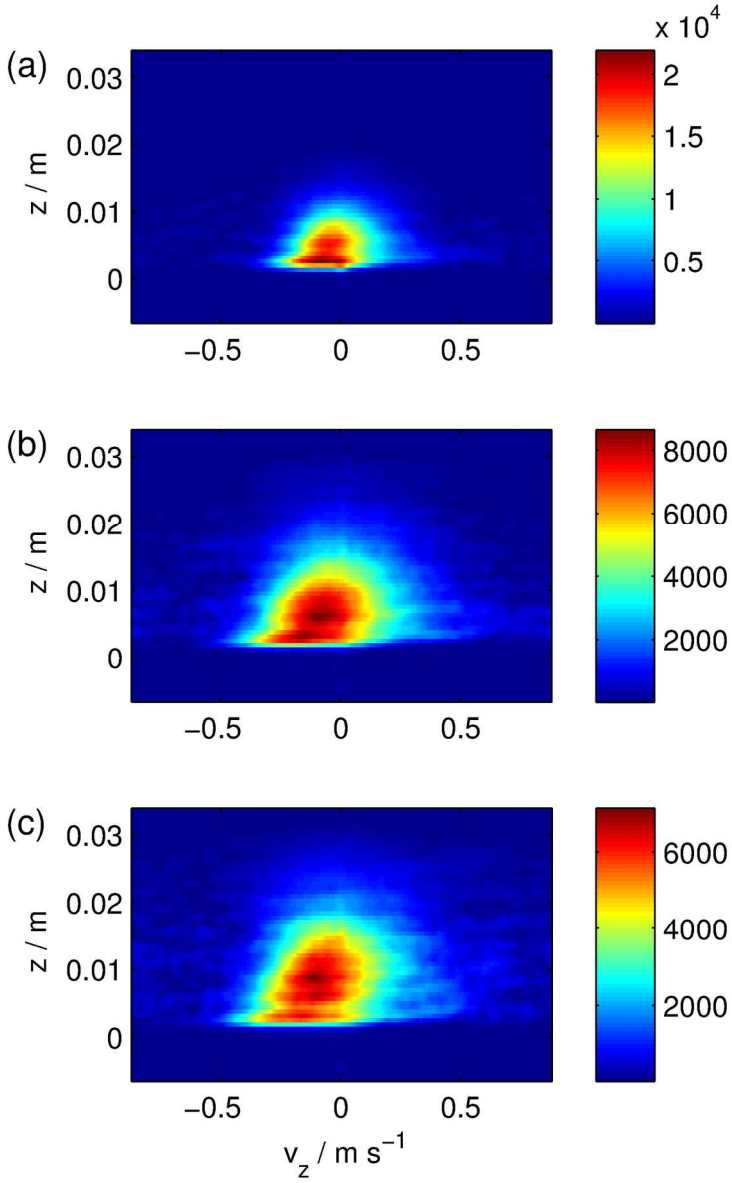

144x234mm (300 x 300 DPI)

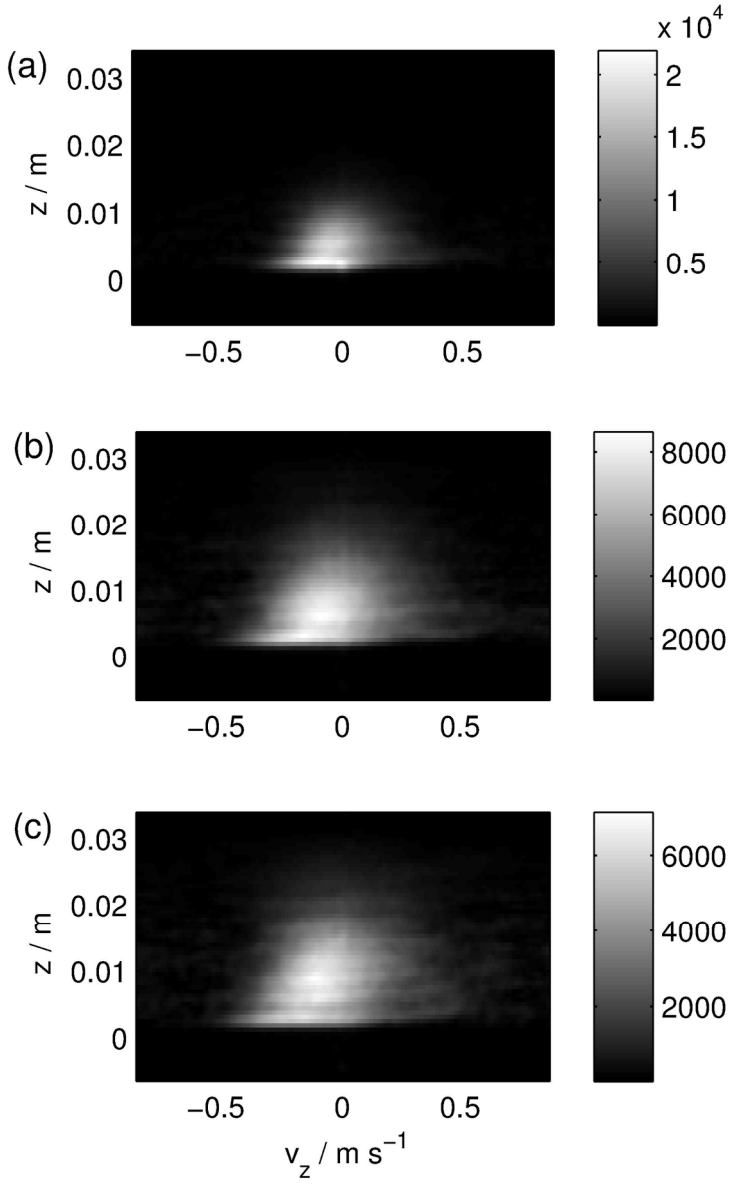

143x233mm (300 x 300 DPI)

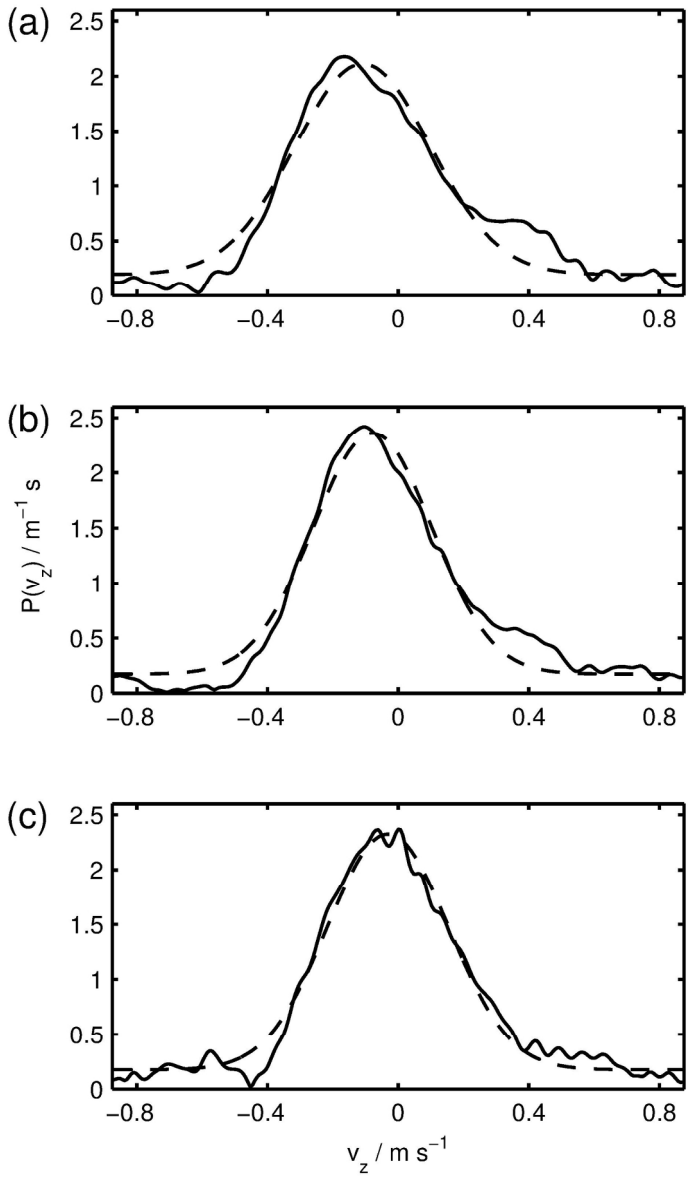

138x238mm (300 x 300 DPI)

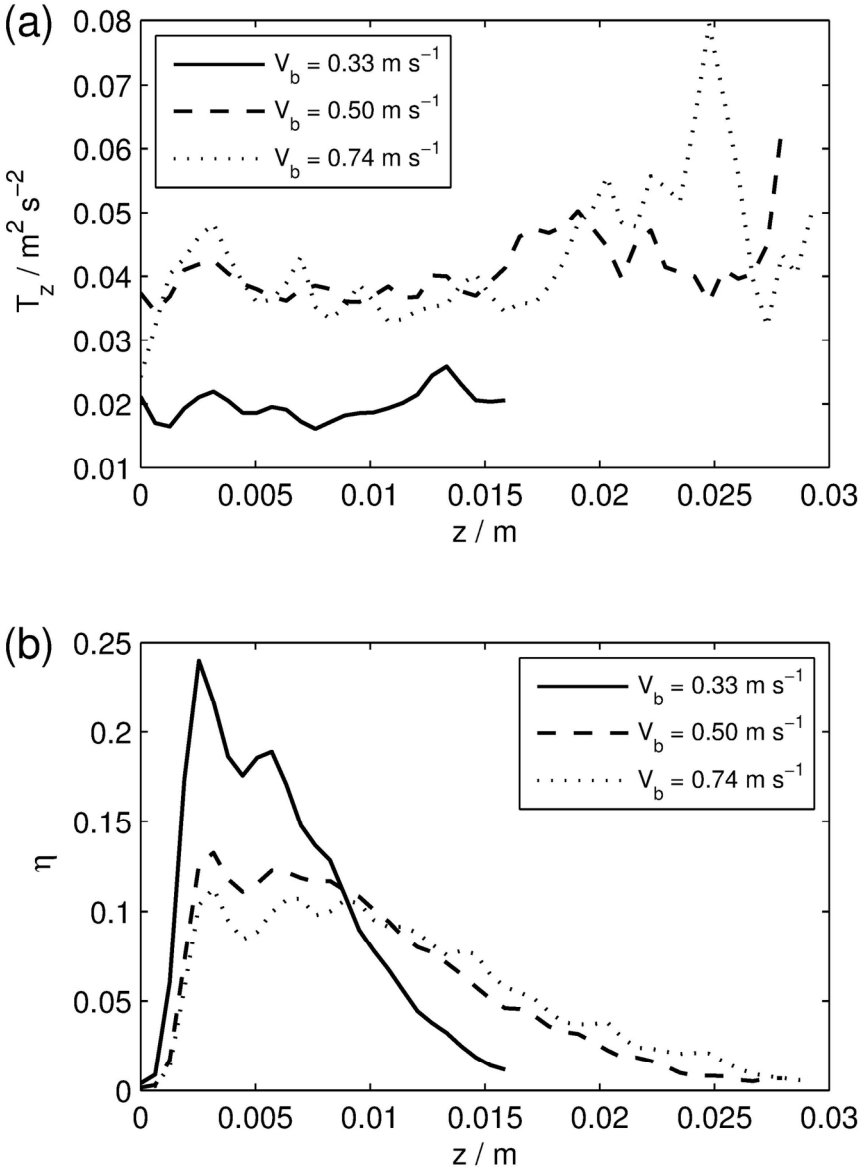

139x190mm (300 x 300 DPI)

Unable to Convert Image

The dimensions of this image (in pixels) are too large to be converted. For this image to convert, the total number of pixels (height x width) must be less than 40,000,000 (40 megapixels).

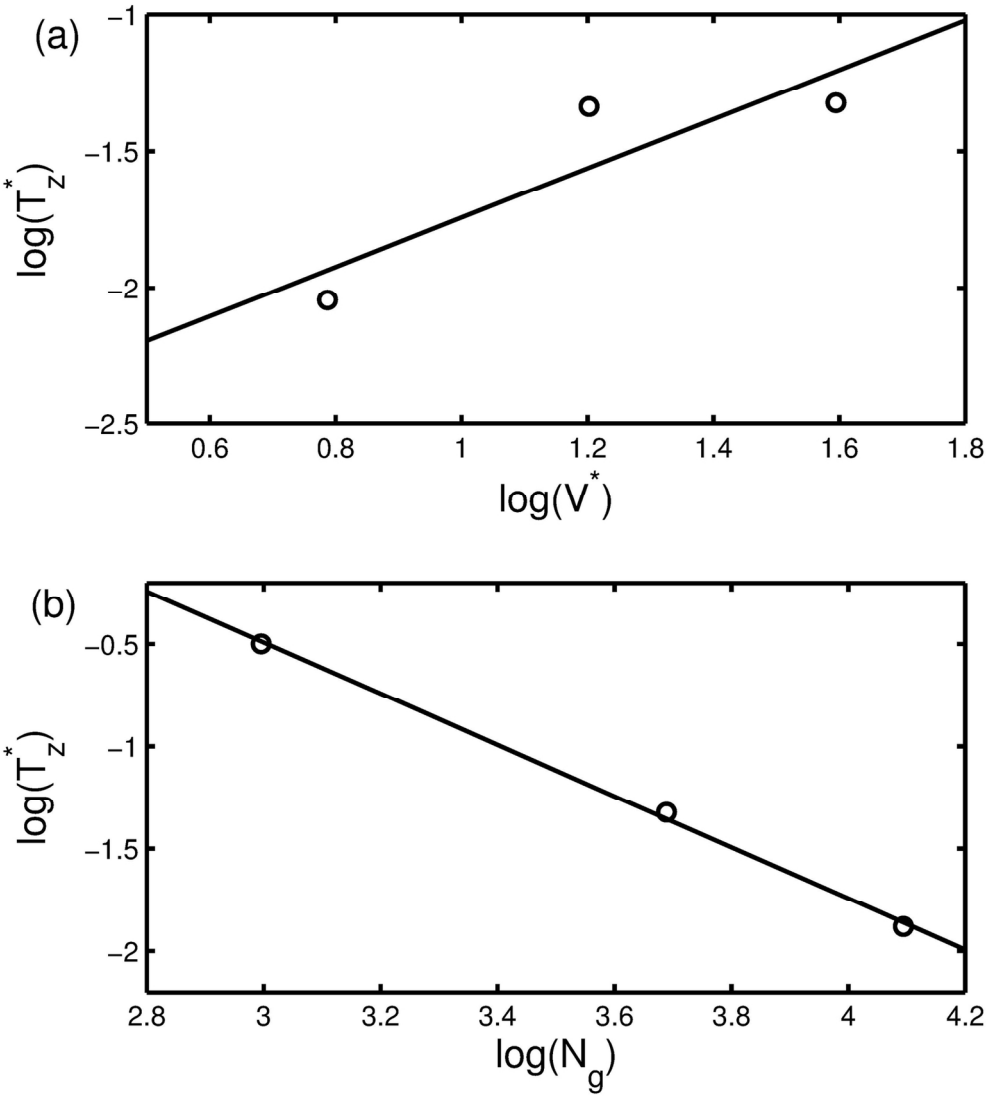

141x157mm (300 x 300 DPI)

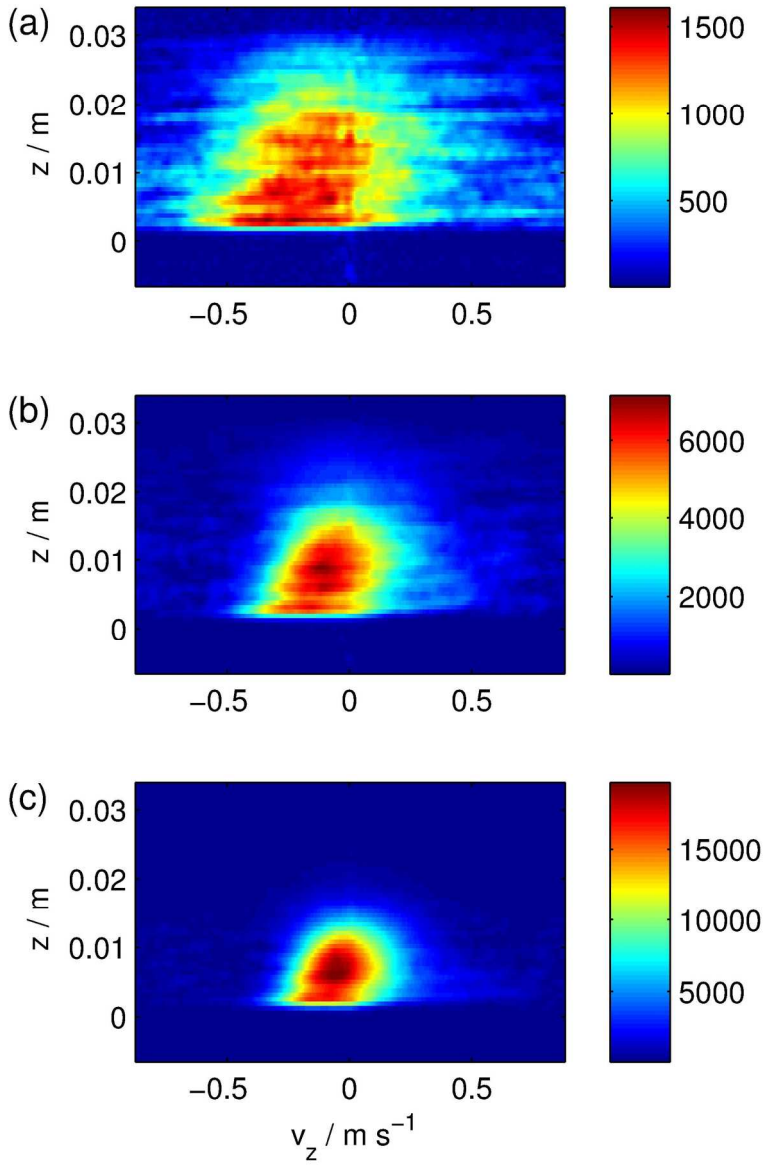

141x219mm (300 x 300 DPI)

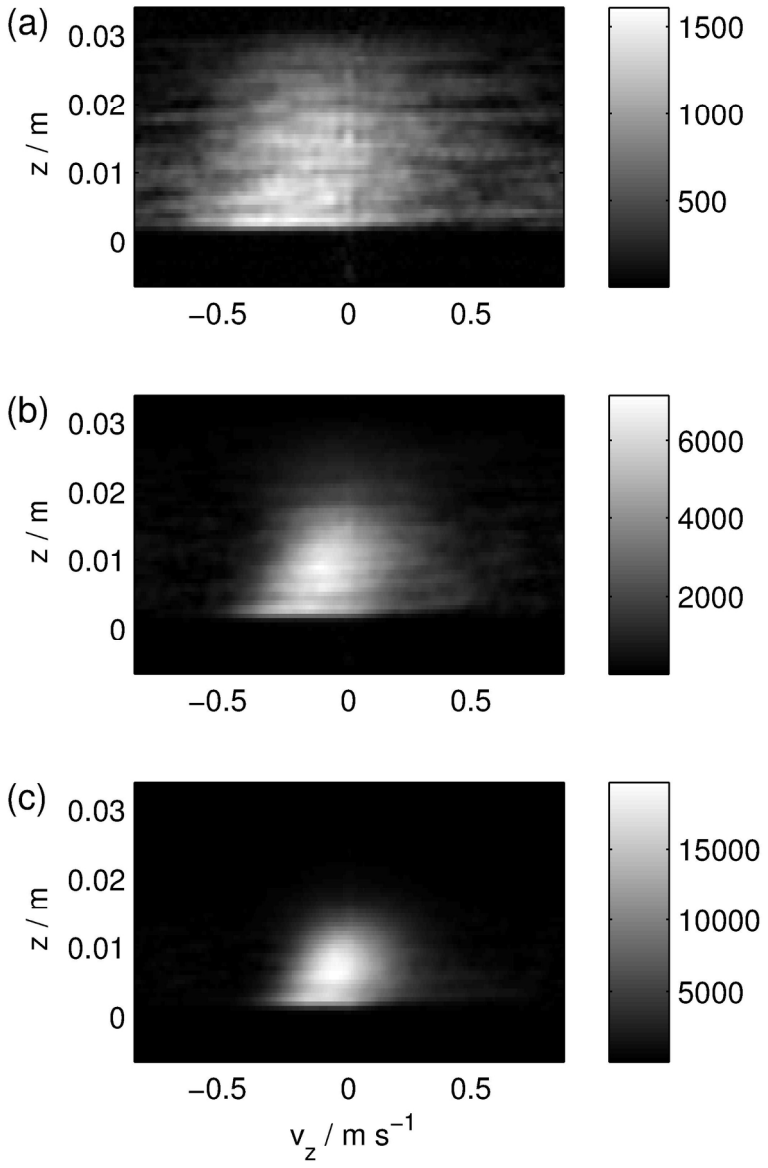

141x219mm (300 x 300 DPI)

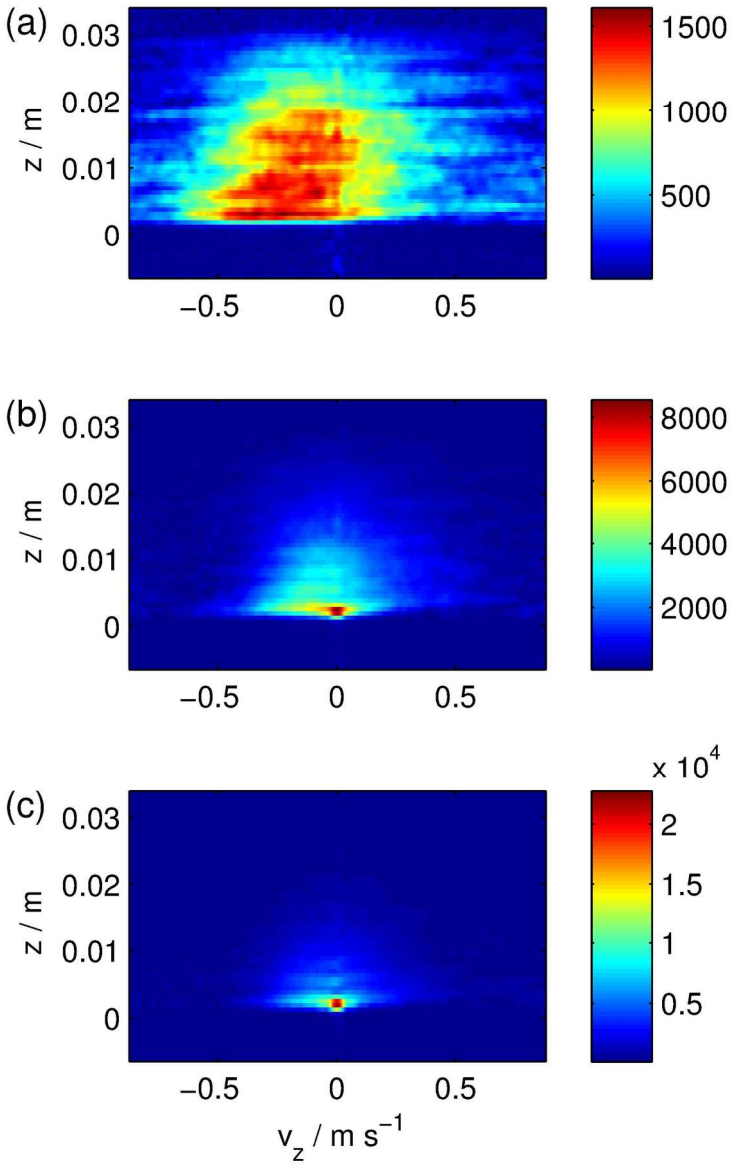

140x226mm (300 x 300 DPI)

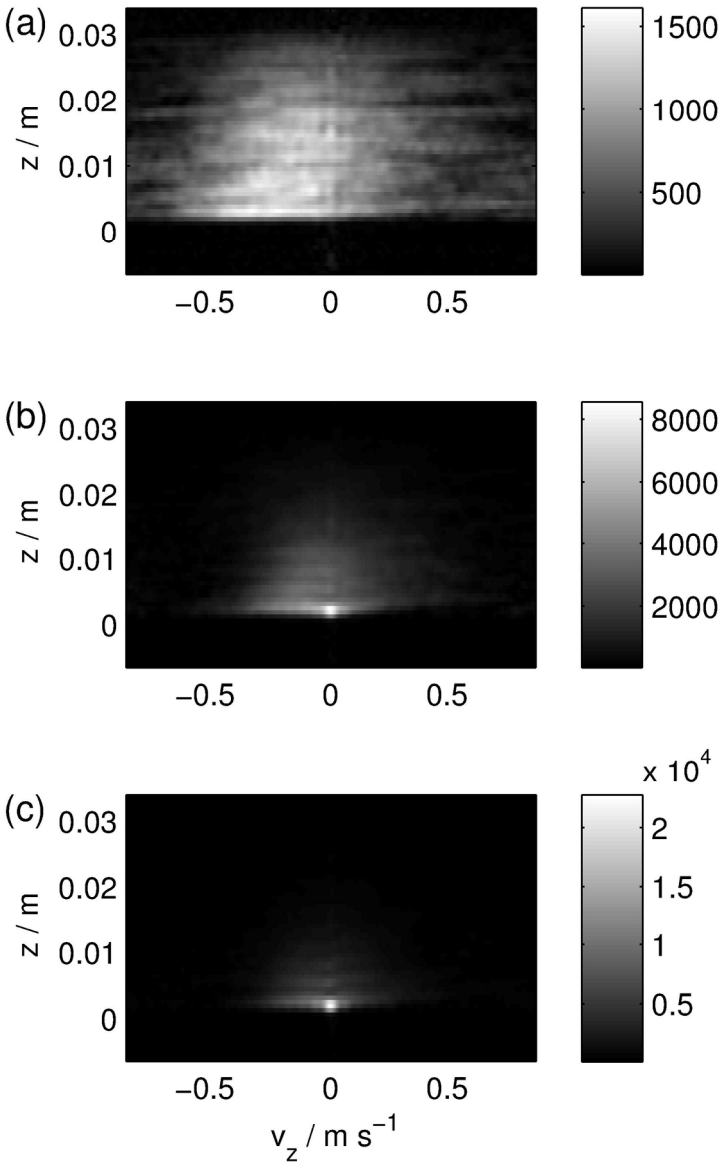

139x227mm (300 x 300 DPI)

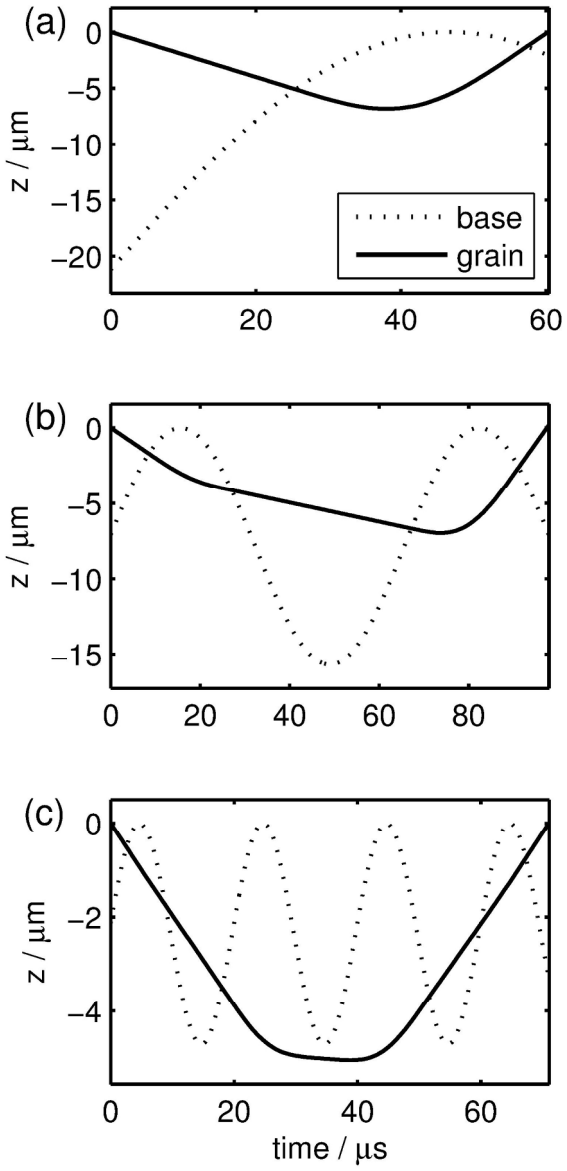

138x285mm (300 x 300 DPI)

Unable to Convert Image

The dimensions of this image (in pixels) are too large to be converted. For this image to convert, the total number of pixels (height x width) must be less than 40,000,000 (40 megapixels).

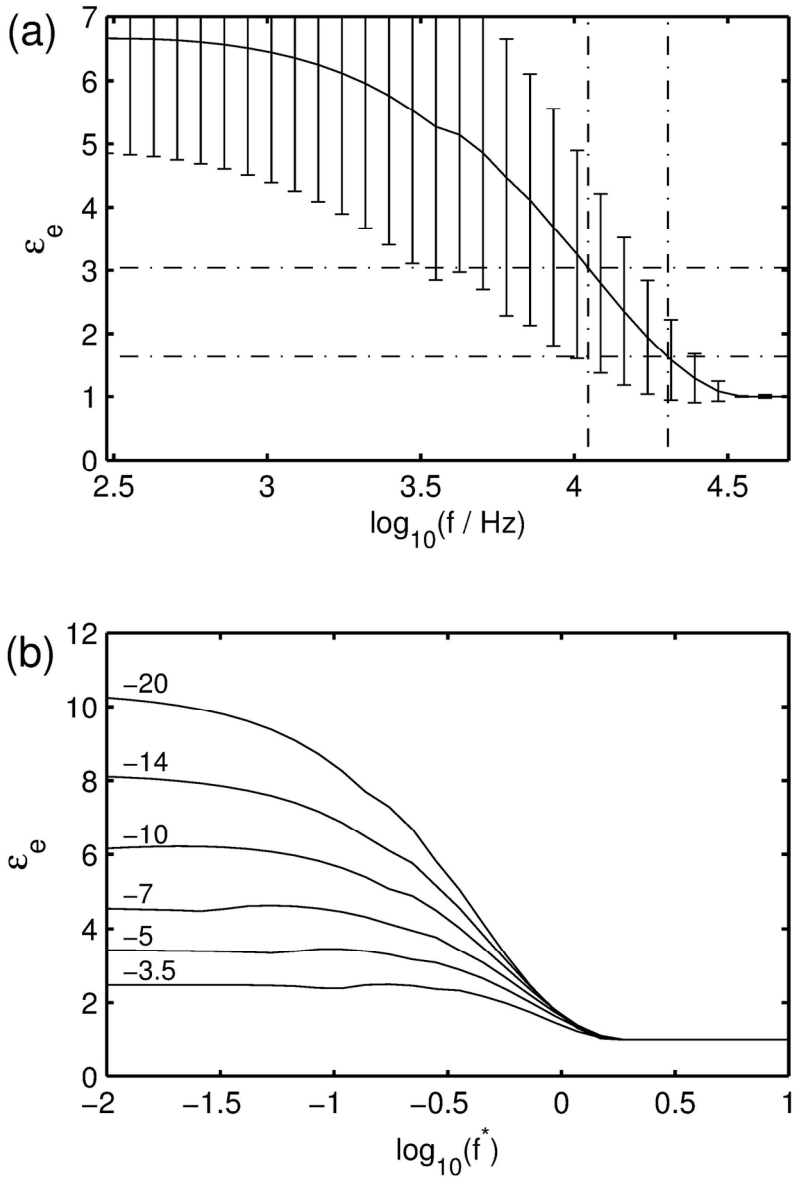

140x204mm (300 x 300 DPI)